

The CDF Archive: Herschel PACS and SPIRE Spectroscopic Data Pipeline and Products for Protostars and Young Stellar Objects

Joel D. Green^{1,2}, Yao-Lun Yang¹, Neal J. Evans II¹, Agata Karska³, Gregory Herczeg⁴, Ewine F. van Dishoeck^{5,6}, Jeong-Eun Lee⁷, Rebecca L. Larson¹, & Jeroen Bouwman⁸

1. *The University of Texas at Austin, Department of Astronomy, 2515 Speedway, Stop C1400, Austin, TX 78712-1205, USA*
2. *Space Telescope Science Institute, Baltimore, MD, USA*
3. *Astronomical Observatory Institute, Faculty of Physics, A. Mickiewicz University, Sloneczna 36, 60-286 Poznan, Poland*
4. *Kavli Institute for Astronomy and Astrophysics, Peking University, Yi He Yuan Lu 5, Haidian Qu, 100871 Beijing, China*
5. *Leiden Observatory, Leiden University, Netherlands*
6. *Max Planck Institute for Extraterrestrial Physics, Garching, Germany*
7. *Department of Astronomy & Space Science, Kyung Hee University, Gyeonggi 446-701, Korea*
School of Space Research, Kyung Hee University, Yongin-shi, Kyungki-do 449-701, Korea
8. *Max Planck Institute for Astronomy, Heidelberg, Germany*

ABSTRACT

We present the COPS-DIGIT-FOOSH (CDF) *Herschel* spectroscopy data product archive, and related ancillary data products, along with data fidelity assessments, and a user-created archive in collaboration with the Herschel-PACS and SPIRE ICC groups. Our products include datacubes, contour maps, automated line fitting results, and best 1-D spectra products for all protostellar and disk sources observed with PACS in RangeScan mode for two observing programs: the DIGIT Open Time Key Program (KPOT_nevans_1 and SDP_nevans_1; PI: N. Evans), and the FOOSH Open Time Program (OT1_jgreen02.2; PI: J. Green). In addition, we provide our best SPIRE-FTS spectroscopic products for the COPS Open Time Program (OT2_jgreen02.6; PI: J. Green) and FOOSH sources. We include details of data processing, descriptions of output products, and tests of their reliability for user applications. We identify the parts of the dataset to be used with caution. The resulting absolute flux calibration has improved in almost all cases. Compared to previous reductions, the resulting rotational temperatures and numbers of CO molecules have changed substantially in some sources. On average, however, the rotational temperatures have not changed substantially ($< 2\%$), but the number of warm ($T_{\text{rot}} \sim 300$ K) CO molecules has increased by about 18%.

Subject headings: Astronomical databases - catalogs - surveys - stars: pre-main sequence

1. Introduction

It has been long established that protostars and young stars form from the collapse of a dense molecular core, developing through different stages as the relative density, temperature, and composition of the envelope, disk, and protostar shift over time. However, many uncertainties remain in the details of the collapse. Specific conditions during infall and outflow throughout the protostellar stage may drive the conditions in the resulting circumstellar disks and protoplanetary systems, influencing the compositional properties of the planet-forming material. Particularly important is the role played by accretion-driven heating events; whether the accretion process is characterized by gradually diminishing accretion (Offner & McKee 2011) or episodic accretion (e.g., Dunham et al. 2010; Kim et al. 2012; Dunham et al. 2014) can have a large impact. In either case, the final disk mass and chemistry may be set by the time spent in relatively high accretion phases; in the case of episodic accretion, the disk mass at the end of the protostellar phase may be determined by the phasing of the last burst of accretion onto the star and the end of infall. Observational constraints on the physical processes in these systems are gained from a multi-wavelength understanding of molecular, atomic, and ionic tracers through optical, infrared, and millimeter-wave telescopes.

Many protostars in relatively nearby ($d \leq 300$ pc) clouds have been studied extensively in the infrared. The Infrared Space Observatory’s Long Wavelength Spectrograph detected gas phase H₂O, high- J CO rotational transitions, and fine structure emission lines toward protostars and related sources (e.g., Lorenzetti et al. 1999; Giannini et al. 1999; Ceccarelli et al. 1999; Lorenzetti et al. 2000; Giannini et al. 2001; Nisini et al. 2002). These lines trace the innermost regions of the protostellar envelope, exposed to heating by the central object, and the outflow cavity region, where winds and jets may interact with the envelope and the surrounding cloud.

The Spitzer c2d (“Cores to Disks”) and Gould Belt Legacy surveys (Evans et al. 2009, Dunham et al. submitted), along with a survey of the Taurus cloud (Rebull et al. 2010), have produced a rather complete list of young stellar objects within 300 pc. These source lists in turn informed key program surveys in the far-infrared and submillimeter, with the Herschel Space Observatory, an ESA space-based telescope with a 3.5-meter primary mirror optimized for far-infrared and submillimeter observations. *Herschel*-SPIRE (Spectral and Photometric Imaging REceiver, 194-670 μ m; Griffin et al. 2010) allowed low resolution spectroscopy over the entire submillimeter domain; the PACS (Photodetector Array Camera and Spectrometer; Poglitsch et al. 2010) instrument provided low-resolution spectroscopy over the far-infrared range. *Herschel* was sensitive to dust continuum, and had access to the full suite of mid- J emission lines from CO, HCO⁺, ¹³CO, and several low-lying energy states of H₂O, which trace the shocked gas in the outflow and the surrounding envelope.

In a previous paper (Green et al. 2013a) we used data from the PACS spectrograph to characterize a sample of well-studied protostars, selected primarily from the c2d sample, including both Class 0 and Class I objects. Class 0 and Class I sources are characterized observationally by rising spectral energy distributions (SEDs) between near-infrared and mid-infrared wavelengths. In addition to the continuum emission, the far-infrared/submillimeter bands contain numerous pure rotational transitions of the CO ladder, as well as low-lying lines of H₂O, OH, HCO⁺, atomic

lines ([C I], [O I]), and ionic lines ([C II], [N II]), all potential tracers of gas content and properties. The transitions and collisional rates of these simple molecules are well-understood (see, e.g., Yang et al. 2010; Neufeld 2012, for a recent update on CO). Thus these lines make excellent diagnostics of opacity, density, temperature, and shock velocities (e.g., Kaufman & Neufeld 1996; Flower & Pineau Des Forêts 2010) of the gas surrounding these systems. In a second previous paper (Green et al. 2013b), we combined PACS, SPIRE, and ground-based spectroscopy of stars undergoing episodic accretion events (FU Orionis objects, hereafter FUors) in order to determine their gas and envelope properties post-outburst. Both previous papers used an earlier data reduction pipeline; we will compare results from those papers to those obtained with the new reduction presented here for a few characteristic quantities in §5.3.

This paper describes the CDF (COPS-DIGIT-FOOSH) archive, with *Herschel*-PACS and SPIRE spectroscopic observations of 70 objects (protostars, young stellar objects, and FUors) from the “Dust, Ice, and Gas in Time” (DIGIT Key Project), “FU Orionis Objects Surveyed with *Herschel*” (FOOSH OT1), and “CO in Protostars” (COPS OT2) *Herschel* programs. These have been delivered to the *Herschel* archive and are available. Here we describe the reduction methods and the data products.

We use data products from the HIPE 13 / CalTree 65 pipeline, provided by the Herschel Science Center, the most current version at the time of reprocessing during summer 2014. The most notable new feature in this reduction of PACS spectroscopy is a correction for pointing and jitter offsets during observations. The SPIRE spectra are also enhanced by the use of a correction for semi-extended sources (Wu et al. 2013). The spectra are reduced and analyzed using automated routines optimized for *Herschel* to detect line emission and continuum properties. We provide spectroscopic data cubes, line fluxes, continuum analysis, and error analysis across all spatial positions observed in these 70 sources. In addition to this paper, a full description of the pipeline and details of this archive can be found in the web release of the data to the Herschel Science Archive (HSA) User Provided Data Products¹, upcoming analysis papers (Green et al., in prep.), and a paper on 3-D radiative transfer modeling of a single source (the protostar BHR71; Yang et al., in prep.). The corresponding *Spitzer* data can mostly be found in IRS_Disks and c2d spectroscopic programs (Lahuis et al. 2006). Finally we note that this analysis could be expanded to include all objects observed in similar modes, and the automated routines adapted to other (non-Herschel) datasets.

2. Observations

2.1. Dust, Ice, and Gas In Time (DIGIT)

The full DIGIT spectroscopic sample consists of 63 sources: 24 Herbig Ae/Be stars (intermediate mass sources with circumstellar disks), 9 T Tauri stars (low mass young stars with circumstellar disks), and 30 protostars (young stars with significant envelope emission) observed with

¹<http://www.cosmos.esa.int/web/herschel/user-provided-data-products>

PACS spectroscopy. The distribution in luminosity and characteristic temperature are shown in Figure 1. DIGIT also included an additional wTTS (weak-line T Tauri star) sample that was observed photometrically and delivered separately. The wTTS sample is fully described by [Cieza et al. \(2013\)](#).

The full DIGIT embedded protostellar sample consisted of 30 Class 0/I targets, drawn from previous studies, focusing on protostars with high-quality *Spitzer*-IRS 5-40 μm spectroscopy (summarized by [Lahuis et al. 2006](#)), and UV, optical, infrared, and submillimeter complementary data. Two sources (IRS44 and IRS46) were observed in a single pointing centered on IRS46. These objects are selected from some of the nearest and best-studied molecular clouds: Taurus (140 pc; 6 targets), Ophiuchus (125 pc; 7 targets), Perseus (230-250 pc; 7 targets), R Corona Australis (130 pc; 3 targets), Serpens (429 pc; 2 targets), Chamaeleon (178 pc, 1 target), and 4 additional isolated cores. The sources span two orders of magnitude in bolometric luminosity, from $L_{\text{bol}} = 0.11$ to $27.8 L_{\odot}$. The photometric fluxes of embedded protostellar sample at 100 μm span two orders of magnitude as well, from 1.0 to 240.1 Jy. In terms of the usual tracers of evolutionary development, the bolometric temperatures range from $T_{\text{bol}} = 27$ to 592 K, spanning the Class 0/I divide at $T_{\text{bol}} = 70$ K. The ratio of L_{bol} to the luminosity at $\lambda \geq 350 \mu\text{m}$ ranges from $L_{\text{bol}}/L_{\text{submm}} = 5$ to > 10000 , with most ratios (18 of 22 with well-constrained submillimeter data) falling between 10 and 1000. The disk sources were selected as bright targets for PACS spectral scans.

PACS is a 5×5 array of $9.4'' \times 9.4''$ spatial pixels (hereinafter referred to as “spaxels”) covering the spectral range from 50-210 μm with $\lambda/\Delta\lambda \sim 1000$ -3000, divided into four segments, covering $\lambda \sim 50$ -75, 70-105, 100-145, and 140-210 μm . The PACS spatial resolution ranges from $\sim 9''$ at the shortest wavelengths (50 μm) to $\sim 18''$ at the longest (210 μm), corresponding to 1000 to 4500 AU at the distances of most sources. The nominal pointing RMS of the telescope is $2''$.

For the DIGIT embedded protostars sample we utilized the full range of PACS (50-210 μm) in two linked, pointed, chop/nod rangescans: a blue scan covering 50-75 and 100-150 μm (SED B2A + short R1); and a red scan covering 70-105 and 140-210 μm (SED B2B + long R1). We used 6 and 4 range repetitions respectively, for integration times of 6853 and 9088 seconds (a total of ~ 16000 seconds per target for the entire 50-210 μm scan). Excluding overhead, 50% of the integration time is spent on source and 50% on sky. Thus the effective on-source integration times are 3088 and 4180 seconds, for the blue and red scans, respectively. The total on-source integration time to achieve the entire 50-210 μm scan is then 7268 seconds.

The telescope and sky background emission was subtracted using two nod positions $6'$ from the source in opposite directions. The telescope chopped between the source and nod positions, cycling every $1/8$ of a second in a pre-determined pattern of on and off positions ([Poglitsch et al. 2010](#)) during the integration.

Most (21 of 33) disk sources were observed with the same procedure as the embedded objects. The other 12 sources have only partial spectral coverage: 8 Herbig Ae/Be sources (HD 35187, HD 203024, HD 245906, HD 142666, HD 144432, HD 141569, HD98922, and HD 150193) and 4 T Tauri sources (HT Lup, RU Lup, RY Lup, and RNO90) were observed using *only* the blue scans

(i.e. achieving a wavelength coverage only from SED B2A + short R1, 100-150 μm). 9 of these 12 sources (all except HD 35187, HD 203024, and HD 245906) were observed in a further limited wavelength range (60-72 + 120 - 134 μm ; referred to as “forsterite only” scans for their focus on the 69 μm forsterite dust feature). This procedure allowed shorter integration times to achieve the same SNR in the covered regions.

2.2. FU Orionis Objects Surveyed with Herschel (FOOSH)

FUors are low-mass pre-main sequence objects named after the archetype FU Orionis (hereafter, FU Ori), which produced a 6 magnitude outburst at B -band in 1936 and has remained close to peak brightness ever since. The FOOSH program consisted of 21 hrs of Herschel observing time: V1057 Cyg, V1331 Cyg, V1515 Cyg, V1735 Cyg, and FU Ori were observed as part of FOOSH and analyzed from preliminary data reduction (Green et al. 2013b).

For the FOOSH sample we again utilized the full range of PACS (50-210 μm) in two linked, pointed, chop/nod rangescans: a blue scan covering 50-75 and 100-150 μm (SED B2A + short R1); and a red scan covering 70-105 and 140-210 μm (SED B2B + long R1). We used 6 and 4 range repetitions respectively, for integration times of 3530 and 4620 seconds (a total of ~ 8000 seconds per target and off-positions combined, for the entire 50-210 μm scan; the on-source integration time is ~ 3000 seconds). The telescope sky background was subtracted using two nod positions 6' from the source.

The SPIRE-Fourier Transform Spectrometer (FTS) data were taken in a single pointing with sparse image sampling, high spectral resolution mode, over 1 hr of integration time. The spectrum is divided into two orders covering the spectral ranges 194 – 325 μm (“SSW”; Spectrograph Short Wavelengths) and 320 – 690 μm (“SLW”; Spectrograph Long Wavelengths), with a resolution, $\Delta\nu$ of 1.44 GHz and resolving power, $\lambda/\Delta\lambda \sim 300\text{--}800$, increasing at shorter wavelengths (Griffin et al. 2010). The FOOSH data were observed in a single pointing with sparse image sampling, high spectral resolution, in 1 hr of integration time per source.

2.3. CO in ProtoStars (COPS)

The sample of 31 “COPS” protostars observed with SPIRE-FTS includes 25 sources from the DIGIT and 6 from the WISH (Water in Star-forming regions with *Herschel*, PI: E. van Dishoeck; van Dishoeck et al. 2011; see also Nisini et al. 2010; Kristensen et al. 2012; Karska et al. 2013; Wampfler et al. 2013) key programs. A nearly identical sample was observed in CO $J = 16 \rightarrow 15$ with HIFI (PI: L. Kristensen) and is presented in Kristensen et al. (in prep.). This dataset (COPS: SPIRE-FTS) is analyzed in a forthcoming paper (Green et al., in prep.). The SPIRE beamsize ranges from 17-40'', equivalent to physical sizes of $\sim 2000\text{--}10000$ AU at the distances of the COPS sources, comparable to the size of a typical core (Ward-Thompson et al. 2007) but smaller than many collimated outflows.

The COPS SPIRE-FTS data were observed identically to the FOOSH SPIRE data, in a single pointing with sparse image sampling, high spectral resolution, in 1 hr of integration time per source, with one exception: the IRS 44/46 data were observed in medium image sampling (e.g. complete spatial coverage within the inner 2 rings of spaxels), in 1.5 hr, in order to better distinguish IRS 44 (the comparatively brighter IR source; [Green et al. 2013a](#), [Green et al., in prep.](#)) from IRS 46.

2.4. Overview of the Products

The basic data products we produce for each source observed with PACS and SPIRE spectroscopy are the following:

- Datacubes (wavelength vs. flux density vs. spatial position), with advanced corrections from HIPE 13.
- Best-calibration 1-D spectra for point sources and marginally extended sources within the data cube, including flat spectra (continuum-subtracted), continuum (line-subtracted), and residual spectra.
- Line identification and fitted parameters obtained with an automated fitting routine (for both 2-D and 1-D spectra), organized by spatial position for each source, including a complete, sortable linelist.
- Contour plots for extended line and continuum emission.
- EPS files for the last three products above, allowing users to verify all automated fits.

In this document, we review the archive data processing and products in detail. First we describe the custom data reduction pipeline we used in §3. Second, we describe the automatic line fitting routine and the line fitting results in detail in §4. Third, we describe the data products and output file format, including post-processing data products in §5. Lastly, we summarize the results of this archive in §6. Our line source libraries and a full inventory of sources included in this archive are shown at the end of this paper, in the Appendix (§7).

3. Pipeline settings

3.1. PACS Pipeline for Pointlike and Small Sources

We begin with the `hipe13.0.1006.ChopNodPointingCorrection.py` pipeline script (the “Point Source Background Normalization” script). This script was made available in HIPE 13; any version of HIPE 13 should work for this purpose. We then made the following modifications:

- The script is run as a loop over numerous OBSIDs for blue and red cameras.

- We make an adjustment in the pipeline to account for the effects of pointing jitter (changes in pointing offset during the course of the observation). The chi-squared difference between the flux of the “point” source and the flux of the centered beam, via a map/grid, is determined using the beams of calibration products. We define the “oversample” (the samples per spatial element in each dimension, improving precision of positional determination) and the “smoothFactor” (smoothing in the spectral domain, in terms of grating positions rather than wavelength). For the pipeline, we set these to oversample = 8 and smoothFactor = 7; using larger values yielded no apparent benefit.
- In the specFlatFieldRange command, we decrease “polyOrder” to 4 (from the default of 5). This slightly improves memory usage, although the effect is minor. There is no impact on the success of the flatfielding.
- We select excludeLeaks = True so that we do not use the light-leakage affected regions for flatfielding. These regions are not reported in the final spectral product, which removes the 95-105 μm range (and a few spectral lines including CO $J = 25 \rightarrow 24$ in that region). The advantage to removing these data is that we avoid the typically erratic continuum in that region when determining the flatfielding correction.
- We change the “gaussianFilterWidth” to 35 (instead of 50). This parameter is the number of wavelength points over which we assess the scaling of the central spaxel to the level of the 3x3 spaxel set, which is used in the production of the “3x3YES” product, below; it is an attempt to correct for the shape of the continuum, picking a width large enough to account for pointing jitter but not so wide as to smooth out the actual continuum shape. By using the flux of the “3x3” central 9 spaxels, and comparing to a true point source distribution, we correct for the movement of the flux centroid throughout the observation, referred to as pointing jitter. The number is essentially based on the sampling and the significance of pointing jitter, for a particular observation; we settled on a value of 35 through trial-and-error testing.
- We add a “garbage collection” line at the end of the loop. This allows us to run at least 200 OBSIDs within a single command, given sufficient disk space. It takes about 1 hour/OBSID to run at these settings on a (early 2014) 12-core processor with 96 GB of RAM dedicated to the process, excluding data download time; for a total of 200 OBSIDs, we required 200 CPU hours (e.g., 2 weeks) to reduce all the targets in our sample.

The default pipeline reduction shows significant mismatches between red and blue modules, and it frequently did not align with photometry or with SPIRE observations of the same position. The early pipelines did not fully account for source spatial extent or pointing jitter, and the relative spectral response function did not work well at the edges of each order (see e.g., [Green et al. 2013a](#)). All of these effects are accounted for in the new pipeline, which has dramatically improved the continuum calibration for PACS in particular. Our new pipeline includes updated calibration data, improved flatfielding, and jitter correction, and other small improvements.

An example of the improvement in spectral/continuum shape, and inter-module flux calibration from the newer pipeline and the jitter correction is shown (for IRAS 12496) in Figure 2. The observations of this source were mis-pointed by about 0.5 spaxel, so it provides a good test. The jitter correction (blue) has removed several spurious broad features and improved overall flux calibration when compared with the non-corrected spectrum (red) or the default pipeline spectrum (black). The absolute flux calibration has also improved considerably. As an example, we consider the improvement to the continuum shape and absolute flux calibration shown for the protostar L1157, a source we will use for most of the following comparisons. Figure 3 demonstrates the improvement. Our best products from the new pipeline results match much better with photometry extracted from archival *Herschel*-PACS and SPIRE imaging of our sample objects in the Herschel Science Archive, from a variety of programs, including: KPGT_pandre_1, KPGT_okrause_1, OT1_jtobin_1, OT1_jgreen02_1, and OT1_mdunham_1. These data were less subject to saturation problems than data from earlier missions or large beam sizes (e.g. *Spitzer*-MIPS, IRAS). The photometry data are extracted with the source size fitted by the spectroscopic (HIPE) pipeline, at the appropriate waveband (70, 100, 160, 250, 350, or 500 μm). The data products from which we extracted our photometry have absolute flux calibration uncertainties of $< 7\%$ for PACS against stellar models (Balog et al. 2014) and asteroid standards (Müller et al. 2014) and 4% for SPIRE when compared against models of Neptune (Bendo et al. 2013), with a 5% uncertainty in cross-calibration between PACS and SPIRE (Müller et al. 2014).

Although L1157 is a typical example, we compared the absolute flux calibration of our final PACS products with the default pipeline products in Figure 4 (top), relative to photometric observations, for all non-confused, protostellar sources of which the photometry was available in the *Herschel* Science Archive – about one third of our sources. The spectra in this archive are convolved with corresponding photometry filters before comparing with photometric data. The data from *Herschel* Science Archive were processed with HIPE 11 by *Herschel* Science Center and collected at mid-2014. The flux is scaled from the spectra of central spaxel to the total flux within the central 3x3 spaxel to match with the flux of our corrected 1-D spectra. The black line indicates a perfect agreement between photometry and spectroscopy; the blue points are values derived from our new products, and the red points are derived from default 2014 HSA products; the enhanced products show much smaller deviation from the photometric values. The products from our archive have a better agreement between the photometry and spectrophotometry. A straight line fitting with data (blue) from our archive shows only a small deviation toward faint sources and without a significant offset to the equality line. Compared to the default HSA products, the dispersion in the residual of line fitting of the CDF products is greatly reduced, from 0.42 to 0.1. The improved reduction has produced reliable spectrophotometry for most sources that are not in confused regions.

Overall, the jitter correction was successfully performed for $\sim 80\%$ of our sources. The advanced pipeline with jitter correction matches the fluxes by matching the minor mispointings at different wavelengths. However, not every spectrum was improved by the correction. Among the embedded sources in our sample, we got very poor results from the jitter correction on 14 sources:

IRAM 04191, L1014, L1455-IRS3, RCrA-IRS5A, RCrA-IRS7C, IRS 46, Serpens-SMM4, EC 82, HD 98922, HD 245906, HD 203024, HT Lup, HD 142666, and HD 35187. The common threads between these sources are twofold: all have either A) complicated PACS fields in which the central source is not the brightest object, or B) weak continuum (< 3 Jy at $60 \mu\text{m}$). For these sources, we include only the “non-jitter corrected” versions in our archive. This method assumes that the lines and continuum are distributed similarly. Lines with very different distribution require special attention (e.g., [Je et al. 2015](#)).

In two embedded sources, we found significant (10%) flux mismatches between the two OBSIDs merged to form the spectrum: L1551-IRS5 (in which the observations were separated by 1.5 yr); and GSS30-IRS1 (which shows complicated behavior at long wavelengths; [Je et al. 2015](#)). In addition, slight mismatches are noted in L1448-MM (a partially blended chain of sources; [Lee et al. 2013](#)).

We find excellent flux matches between modules in all other sources, including all disk/point sources, even in cases with up to 0.5 spaxel mispointings (e.g. TMC1A, IRAS 12496, TMR1, and L1527). Note that we apply no “by-hand” manual scaling after the pipeline reduction.

3.2. SPIRE Pipeline for Pointlike and Semi-Extended Sources

SPIRE used an FTS spectrometer with an onboard calibration source; separate modules were used for short (SSW) and long (SLW) wavelengths. Each module was reduced separately within HIPE version 13.0 using the standard pipeline for extended sources, including apodization. Originally, SPIRE had a spectral resolution of 1.2 GHz. Because the signals are recorded in the Fourier domain, the line would appear as a sinc function with a spectral resolution of 1.2 GHz. After apodization, the spectral response becomes Gaussian-like, but the spectral resolution is degraded to 1.44 GHz.

Unlike the case of the PACS pipeline, no significant modifications were made to the basic pipeline script, except for allowing it to run in a loop and for the separate post-processing step to improve the calibration for semi-extended sources. The SPIRE data were extracted using the “extended source” calibration pipeline, as this produced a smoother continuum between modules, better signal-to-noise ratio (SNR), and fewer spectral artifacts than the “point source” pipeline (Figure 5). We performed post-processing within HIPE version 13.0.1006, using SPIRE calibration dataset 12. Starting from the baseline data products, we used the “SemiExtendedSourceCorrector” script, which minimizes the mismatch between SLW and SSW. This semi-extended source correction calibrates sources that are partially resolved by the SPIRE beam. The correction fits a source size based on the assumed source profile to minimize the ratio of SLW and SSW at the overlapped wavelength and then calculates the spectrum within a $40''$ Gaussian reference beam, which is independent of wavelength ([Wu et al. 2013](#)). This procedure greatly improves the match of the two modules within SPIRE (as it was designed to) and also smooths the continuum (compare Figure 5 and Figure 15 (bottom) for L1157). We applied the “semi-extended source” calibration to all but a few sources (HH 100, IRS 46, and V1735 Cyg) that were excluded owing to their poor spectral

quality.

The SPIRE spectrophotometric and photometric fluxes, when extracted in the same reference beam, match to within 5% in 21 of 32 protostars and 2 of 3 FUors. The other 12 sources show varying degrees of mismatch with the photometry. The spectra of B1-a, GSS 30-IRS1, IRAS 03301, and L723-MM overestimate the photometry by 10-20%; the reverse is true for L483 and IRAS 15398; these are within formal uncertainties for the spectral flux calibration, and are likely attributable to complicating extended emission. V1331 Cyg shows a larger mismatch at 250 μm , exceeding the photometric point by 50%; the arclike extended structure associated with this compact source may be the cause. The 250 μm photometry for WL 12 and L1455-IRS3 seems suspect. Finally, the IRS 44/46 combined field cannot be fully disentangled; the “IRS 46” SED is contaminated by IRS 44 for $\lambda > 70 \mu\text{m}$; the “IRS 44” SED is missing substantial flux at all wavelengths due to the position of IRS 44 near the edge of the PACS field-of-view.

Figure 4 (bottom) shows the comparison of 21 sources for which we gathered photometry data. The spectrophotometry from the spectra from the Herschel Science Archive default product (collected in mid-2014) are roughly a factor of 4 lower than the photometry. The spectrophotometry from our archive (benefitting from the semi-extended source correction processing), shown in blue, agrees significantly better with the actual photometry. Separate fits to the HSA product spectrophotometry and our product spectrophotometry have similar slopes, which do not match the line of equality. The increasing deviation at faint sources is therefore not caused by the semi-extended correction but derives from the uncorrected spectral data. Note that the scatter in the fit residual is nearly identical – 0.19 for HSA products and 0.18 for CDF products.

We also find improved agreement with previous ground-based submillimeter data. We compared the filter-convolved spectrophotometry from this archive with SPIRE photometry for almost all SPIRE sources in this archive and SCUBA/SHARC-II total flux for the sources from Shirley et al. (2000), Young et al. (2006), and Wu et al. (2007). The mean ratio of spectrophotometry from this archive over the flux measured by SCUBA/SHARC-II is 1.19, while the mean ratio measured from the spectrophotometry from the Herschel Science Archive is only 0.38. The scatter in the residual subtracted with the fitted line is 0.11 for HSA products and 0.09 for CDF products.

The semi-extended source correction has greatly improved the SPIRE spectrophotometry, but it has introduced an offset between the longest wavelength in the PACS data and the shortest wavelength in the SPIRE data, which usually has more emission than the extrapolated PACS data (Fig. 9). This problem arises from the fact that the semi-extended source corrector assumes a source size that is constant with wavelength and because no background subtraction was performed. In bright extended sources, the mismatch is systematic as noted above. In fainter sources (those with 200 μm intensity $\lesssim 25 \text{ Jy}$, the SPIRE flux exceeds the PACS flux by a factor of three on average. The protostars in our sample are typically resolved (marginally) by SPIRE, and their spatial extent increases with wavelength. As the corrector assumes a source model that is independent of wavelength, it overpredicts the flux at short SPIRE wavelengths; thus the SPIRE flux for $\lambda \lesssim 300 \mu\text{m}$ is too high for extended sources. Improving this result requires knowledge of source inten-

sity distribution as a function of wavelength. We apply a 3-D radiative transfer model to explore this issue for one protostar in an upcoming paper (Yang et al., in prep.), but, lacking models for all sources, our archival products cannot account for this effect. The SPIRE spectrum should be considered an upper limit to the true flux density at the shortest wavelengths.

4. Automated Line-Fitting

We use an automated emission line fitting process (available at [GitHub²](https://github.com/yaolun/Her_line_fit)) that tries to fit lines from a pre-existing database of laboratory wavelengths, identifies the threshold for detection, then generates tables of line flux, width, centroid, and uncertainties for every detected line, along with an upper limit to the flux for every undetected line for all PACS and SPIRE spectra in the sample. This information is then combined with spatial information for each pixel to produce contour maps including all spatial positions where significant detections are found. The line-fitting algorithm uses `mpfit`, a Levenberg-Marquardt non-linear least squares minimization (Markwardt 2009), to determine emission line properties. After producing a line detection database, we test the integrity of the line fits to better characterize the SNR, decouple any blended line, and produce easily searchable products for further science applications. The automated results have been spot checked by eye but should be used with caution. In particular, lines that are distributed very differently in space from the continuum emission, or sources in complex regions will need special consideration. The detailed procedures are described in the following sections and an overview of the process is shown in Figure 8.

4.1. Line List

A comprehensive and pre-selected line list is used to supply initial fit parameters for the automated routine. We require an expected line list to restrict our line fitting to specific regions of the spectrum, pre-select line-free continuum regions, and identify the lines after fitting. For this dataset, we verified that there were no significant unidentified lines. If the input spectrum contains a line that is not included in our list, one can easily check whether every significant feature has been extracted from the spectrum: any line not included in the linelist will then appear in the residual spectrum (see §5). The line list includes lines of CO, ¹³CO, H₂O, OH, HCO⁺, CH⁺, and atomic fine-structure transitions in the wavelength range of 55-670 μm (Tables 2, 3, 4, 5, and 6). Table 7 lists potentially blended lines that are fitted with double Gaussians (see §4.4). Two CH⁺ lines, CH⁺ $J = 4 \rightarrow 3$ and CH⁺ $J = 2 \rightarrow 1$, were excluded because they are heavily blended with nearby potentially strong water lines.

The laboratory data for each line were collected from the Leiden Atomic and Molecular Database (LAMDA; Schöier et al. 2005) and the Cologne Database for Molecular Spectroscopy

²https://github.com/yaolun/Her_line_fit

(CDMS; Müller et al. 2005). However, the CO $J = 48 \rightarrow 47$ to CO $J = 41 \rightarrow 40$ lines were not included in LAMDA until recently; thus we calculated the frequency and Einstein-A coefficient using a method from Authier et al. (1993) and the model of the dipole matrix element in Goorvitch (1994). An updated CO extrapolation added to LAMDA (Neufeld, in prep.) agrees with our calculations. We use slightly different line centroids of OH lines, adopted from Wampfler et al. (2013). The only difference is the line centroid of OH ${}^2\Pi_{1/2, 3/2}^+ - {}^2\Pi_{1/2, 1/2}^-$; we use $163.12 \mu\text{m}$ instead of the value of $163.019 \mu\text{m}$ from LAMDA. We use only subsets of the line list within the wavelength range of the observations for each specific source. Finally, we note that [N II] $122 \mu\text{m}$ and $205 \mu\text{m}$ do not appear in the LAMDA database, and there is a discrepancy between the centroid reported in the ISO-LWS line list (taken from the SMART data reduction package, Higdon et al. 2004) and the line list from Peter van Hoof (<http://www.pa.uky.edu/~peter/atomic/>). We used the line centroids from the ISO line list as initial guess, but allowed the line centroids to vary up to ± 2 spectral resolution to determine better values. The averaged fitted line centroids of two [N II] lines from all detections with $\text{SNR} > 10$ are $121.911 \mu\text{m}$ and $205.170 \mu\text{m}$. In Table 6, we report the mean values and the standard deviation of the mean of two [N II] lines. Figure 6 shows the detected [N II] $122 \mu\text{m}$ and [N II] $205 \mu\text{m}$ lines found in this archive.

4.2. Baseline Selection and Fitting

Before fitting each line, we select a nearby spectral region without line emission, from wavelengths near the theoretical line centroid (hereinafter referred as “line-region”) and use this region for baseline fitting. The baseline fitting region is 10 times the spectral resolution at the wavelength of the line centroid. However, some of these wavelengths may include other emission lines. Thus we use only line-free wavelengths (determined from our previously constructed line list) until we have accumulated 5 times the spectral resolution, both blue-ward and red-ward of the line centroid. Then, we fit the selected baseline region using a second order polynomial. Once we obtain a well-constrained baseline, we subtract the baseline from the identified wavelength region. This continuum-subtracted spectrum is then used for line-fitting.

4.3. Line Selection and Fitting

We begin with the baseline-subtracted spectrum. The next step is to extract the line profile, using a Gaussian model. Several constraints are applied to the fitting process for PACS and SPIRE spectra. First, the line centroid is allowed to vary within ± 2 times the spectral resolution at the theoretical line centroid except for the [O I] line at $63.18 \mu\text{m}$. Because this line appears to have real velocity shifts in some sources, presumably due to wind motions, the line centroid is allowed to vary within ± 3 times the spectral resolution instead. Secondly, the linewidth is flexible in the fitting for SPIRE spectra, while the linewidth is fixed at the instrumental resolution for PACS spectra. The spectral resolution of PACS was insufficient to resolve most of the lines except for the [O I] line at $63.18 \mu\text{m}$. The linewidth of [O I] $63 \mu\text{m}$ line is allowed to vary from -30% to 50% because this

line may be broadened by the associated outflows. After comparing the fitting results with and without the linewidth fixed at the PACS instrumental resolution, we found that both strong lines and weak lines can be identified in the fixed-width setting with moderate SNR, while the flexible width setting produces better SNR on strong lines but might fit a narrower than reasonable feature at some wavelengths. The SNR of a strong emission line fitted with a flexible width shows only a 6% increase compared to the SNR of the same line fitted with fixed-width setting. Therefore, for all lines other than [O I], we fix the FWHM of the line to the PACS spectral resolution. Users might be able to achieve a higher SNR, but we adopt the fixed width setting to avoid fake lines in this archive. For SPIRE, similar problems are not found due to a higher oversampling rate; thus we keep all line widths flexible within $\pm 30\%$ of the SPIRE instrumental resolution. The instrumental resolution of PACS was obtained from personal communication with Dr. Helmut Feuchtgruber from MPE/Garching, and the instrumental resolution of SPIRE was obtained from the SPIRE data reduction guide released by *Herschel*.

4.4. Blended Lines Fitting: Double Gaussian Fitting

Some emission lines are sufficiently blended that our default single Gaussian profile does not characterize the line shape. For known blended lines (listed in Table 7), we use a double Gaussian function to fit the blended profile. We only fit a double Gaussian model to two blended lines, while cases of more than two blended lines are fitted with a single Gaussian model for each component and labeled with blending condition (see next paragraph). The width of each component of blended lines are fixed to the instrumental spectral resolution. For blended lines, we require that both lines are in emission; if an absorption line is blended with an emission line, it cannot be fitted. When the fitting routine reached the boundary and tried to fit a negative value to the line height, this value would be set to zero, resulting in a zero line flux in the report. Note that line fitting with a single Gaussian profile does allow negative flux values; this restriction on negative line flux values was only necessary for blended lines.

In the cases that a double Gaussian profile is not sufficient to distinguish two lines, the fitting process fits each line with a single Gaussian profile. If a detected single line can feasibly be identified with either of two lines in our linelist, depending on the physical properties or chemical composition of the source, we use a simple criterion to identify the possible blended regions as well as the likely dominant line. For any pair of lines with centroids located within one resolution element of each other, we classify the fit as a possible blended line, label the two options with Red and Blue indicating whether we attribute the blended line to the longer or shorter wavelength candidate. If a given line is not blended, we label it as x; if a line is blended with two other possible lines, the line is flagged with Red/Blue. Our *recommended* line identification is simply the line with the highest Einstein-A coefficient, as the level population dependence on physical conditions can be complicated. These blended lines are typically water lines with similar excitation requirements. These recommendations for line identification are recorded as 1 in the column `Validity`. These suggested identifications should be used with caution.

We show two examples of double Gaussian fitting in Figure 7. In the top panel, we fit partially blended CO and [C I] emission lines. The bottom panel shows p-H₂O and CO emission lines. In the first case, the fitting algorithm successfully resolved the blended lines, and both will be listed in the table of fitting results (see § 4.6). In the second case, only the CO $J = 18 \rightarrow 17$ line is detected, so the CO line will be reported as a detection and the p-H₂O line as a non-detection.

In some spectral regions, there are three possible line candidates. We do not fit any triple Gaussian profiles due to the instability of such fits. Those lines are labeled in the same fashion. These regions will require individual fits with some a priori knowledge of the likely relative strengths of the three lines.

4.5. Noise Estimation

The problem of noise estimation is two-fold. An accurate evaluation of the uncertainties of the fitted parameters needs a reliable uncertainty for each spectral data point. However, no uncertainties are provided for the SPIRE data, and those supplied for PACS are unrealistic. Therefore, the uncertainties of the spectral data points need to be estimated from the spectrum itself. After the baseline fitting, the fitting process proceeds in two ways, one for full SED scans and one for short scans (§2). We will describe the process first for the full SED scans (the majority of the sources) and then describe the changes needed for the sources with only short scans.

For sources with full SED scans, we feed the fitting routine with the spectra three times, two to precisely measure the uncertainties from the fluctuations of the baseline (hereafter baseline noise) and one to apply the baseline noise as the uncertainties of the spectral data points to get an accurate evaluation of the uncertainties of fitted line parameters (Figure 8). The baseline noise is fed into the final fitting process to get the final fitted parameters with uncertainties. Each time the lines are fitted, the SNR of the line flux (F_1) is calculated by taking the line strength divided by the standard deviation of the modified baseline (the baseline with continuum removed) times the square root of the oversampling rate and the FWHM of the line and 1.064 for a Gaussian profile (Equation 1).

$$\text{SNR} = \frac{F_1}{1.064 \sigma_{\text{baseline}} \sqrt{\text{oversampling}} \times \text{FWHM}} \quad (1)$$

During the first pass through the data (left panel of Figure 8), the routine attempts to identify and remove all lines in the line list and calculates a first estimate of the SNR using a restricted baseline range (± 10 spectral resolution elements around the line centroid). This modification is designed to include enough wavelength channels in the baseline while avoiding contamination from nearby strong lines. It is a rough estimation, which will be refined if the full noise estimation process can be performed.

In the first fitting process, every line is fitted without any prior knowledge of other lines. This first estimate occasionally yields anomalous uncertainties for blended lines or lines with other lines nearby, as the residual after subtracting the fitted line is not only the noise but also other, not-

yet-fitted, emission lines. Thus in the second pass of the data, we subtract all lines identified with $\text{SNR} > 2$ (SNR calculated from the noise biased by not-yet-fitted lines) from the whole spectrum. Then we use a top-hat smoothing function to approximate the continuum shape. We then subtract the continuum to produce a residual spectrum without any contamination, which is the main goal of the second pass (middle panel of Figure 8).

With the improved estimation of the uncertainties of the data points in hand, a third line fitting is executed (right panel of Figure 8), producing reliable uncertainties of fitted parameters. The extra two steps in the line fitting routine increase the SNR by 23% (38% for strong lines). The smoothing function and continuum subtraction are also applied during the third fitting. The SNRs are calculated from the residual spectra from the third fitting. The fitting results produced from the third fitting, as well as the continuum, flat, and residual spectra, are those reported in the archive (examples in Figure 9). The continuum spectrum is the best product for modeling dust continuum emission. The flat spectrum provides an overview of the line emission, and the residual spectrum can be examined for unidentified lines or anomalies in the line fitting process.

For the short scan sources, the continuum coverage is insufficient to derive a complete continuum spectrum; consequently the estimate of the baseline noise is less precise and nearby lines could be adding to the noise. The second fitting process for those data uses the noise estimated from the first pass as the uncertainties in the fitting process to derive the fitted parameters with uncertainties. There is no third pass for those sources. The fits with all three fitting processes are labeled as “Global”, while the ones with only two fitting processes are labeled as “Local” in the “full_source_list.txt” file (see §4.6).

By feeding in realistic uncertainties of the spectra, we can calculate reasonable uncertainties in the fitted parameters of the line. In Figure 10, we show the relation between the two different uncertainties, the uncertainty from the baseline and the uncertainty in the fitted line flux. Most uncertainties calculated by both methods correlate well with each other, for both PACS and SPIRE data, verifying that the uncertainties are correctly processed in the fitting routine.

While the uncertainties determined by each method (baseline fitting and line fitting) are similar (marked by a “line of equality”), there are some interesting features. In both figures, the points spread over about two orders of magnitude, partly reflecting the higher noise in some modules (see Figure 3 for example) and partly due to the changing FWHM in wavelength space, especially for SPIRE. The distributions of the uncertainties measured in different modules of both PACS and SPIRE show a Gaussian-like distribution with a tail toward higher uncertainty. For PACS, the uncertainty distribution of each module centers at different values with B2A highest, B2B in middle, and R1 lowest. The two R1 modules have a similar distribution, although the data are processed separately. For SPIRE, the SLW module has an uncertainty distribution peaking at a lower value compared to SSW. Finally, there is a spread of fits that lie above the line of equality reflecting the fact the the assumed line profile is not always a good fit to the data.

4.6. Reporting of Line-fitting Results

The results from the fitting routine are written in the folder called `advanced_products`, part of the archive structure described in §5. The results include information on the fitted line parameters, as well as the flat spectrum, pure continuum spectrum, and residual spectrum (Figure 9). The offset between PACS and SPIRE spectra is discussed in Section 3.2. Guidelines for properly interpreting the report are discussed below.

These text files are named `object_reduction_trim_lines.txt`, and they contain all of the information necessary to reconstruct the line fits. These ASCII table contains either 18 or 19 columns (for the 1-D spectrum or the spectrum of a single spaxel, respectively).

There are some caveats that should be considered before applying the results. Note that every line checked for a fit is listed, so many will be non-detections. Choosing a suitable minimum SNR would be necessary to select likely detections. Then further quality control checks should be applied. First, the “`Validity`” column should be 1 for each unique plausible line detection. If an uncertainty column indicates `-999`, the fit was unsuccessful and the fitted parameter and its uncertainty value should not be used; all lines flagged with `-999` in any column should be discarded. The `-999` flag is applied to the columns of `Sig_Cen_WL(um)` and `Sig_FWHM(um)` if the quality of the fit is poor. This flag indicates that the line profile reached the local χ^2 minimum by moving to the edge of the allowed parameter space, stopping only due to imposed fitting constraints. In this case, the fitting routine is probably not identifying the input emission line. We do not recommend using any line flagged as 0 in `Validity` or `-999` in other columns, except for the [O I] 63 μm line, which can be wider than expected. We *strongly encourage* users to check the fitting plots of [O I] 63 μm lines before applying the results.

If an uncertainty column is flagged as `-998`, the fitted parameters can be used, but the uncertainties will need to be extrapolated from other nearby line fits. The `-998` flag appears only in the uncertainty columns `Sig_FWHM(um)`, `Sig_Cen_WL(um)` and `Sig_Str(W/cm2)`, and only if the line width is fixed to a particular value (the instrumental resolution at that wavelength). In this case uncertainties cannot be generated, but the fitted parameters are considered reliable. We fix most line widths in PACS line fits (an exception is [O I] 63 μm , which has been observed to be broader than the instrumental line width), but only fix the width for cases of double-Gaussian fitting in SPIRE line fits. In these cases of fixed line width, we cannot calculate uncertainties for the line width. If an uncertainty is needed, we recommend using values for a nearby line if available. A portion of the fitting results table is shown in Table 8; the full table is available in the online manuscript.

A summary of sources and how they were processed can be found at “`full_source_list_refine.txt`”. It lists the names of the processed sources in order and the status of access to different reductions. Additional information can be found in the file “`full_source_list.txt`”, which includes the information about the noise re-estimation (see §4.5).

In total, we performed line fitting on 67 and 33 objects in the PACS and SPIRE bands, respectively. 2-D PACS datacubes consist of four modules of 25 spaxels each, and SPIRE datacubes consist of two modules of 33 and 19 spaxels, for SSW and SLW respectively. Including all spaxels in the 2-D datacube, totaling 264590 PACS and 60330 SPIRE line fitting processes, we found 10474 and 4985 detections without any anomaly in PACS and SPIRE fits, compared to 254116 and 55345 non-detections, including anomalies (fits with $\text{SNR} > 3$ but a flag for poor fitting quality applied). Any line fit in which an unphysical broad component was fitted, the line centroid diverged and reached our pre-defined boundary, or the fitted line was blended with another line with lower Einstein-A value, was determined to be an anomaly. There were a total of 322 and 1334 anomalies in the PACS and SPIRE fits. On average, we found 156 and 151 lines per object in PACS and SPIRE bands, including all spatial positions. The fitting results of all PACS and SPIRE sources are also stored in four ASCII files for 1-D and 2-D spectra (“CDF_archive_pacs[spire]_1d[cube]_lines.txt”).

4.7. Contour Plots

To further visualize the fitting results, we produce contour plots of each line (line contours) overplotted on the local continuum at the wavelength of the line centroid (e.g., Figure 11). We plot contours only for maps with detections in *more* than 2 spaxels; however, plots with continuum emission are provided for maps with fewer detections. The contours are the minimum curvature surface interpolated from lines with SNR greater than 3. The adjacent contours are in steps of 20% of the peak, while the lowest 20% contour is not shown. The crosses (white) in each figure indicate the physical position of each spaxel and the center cross indicates the pointing position. The crosses marked in green indicate spaxels with significant line detections; users can judge the reliability of detailed structure in an individual contour plot based on the number and location of spaxels with detections.

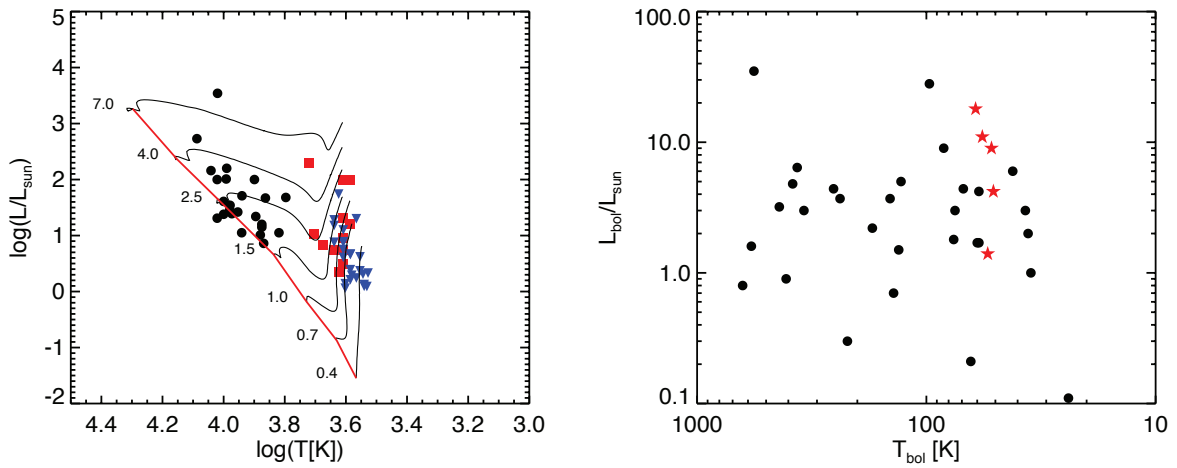


FIG. 1.— **Left:** Range of stellar temperature and L_{bol} for the disk sample, superimposed on the HR diagram with evolutionary tracks by Palla & Stahler (1993). The filled black circles indicate our Herbig Ae sample, the red squares indicate the HR diagram positions of our classical T Tauri star (cTTS) sample, and the blue triangles denote the positions of our wTTS sample. **Right:** Range of T_{bol} and L_{bol} for the embedded sample. Red stars indicate sources observed by the “WISH” key program with PACS full spectral scans.

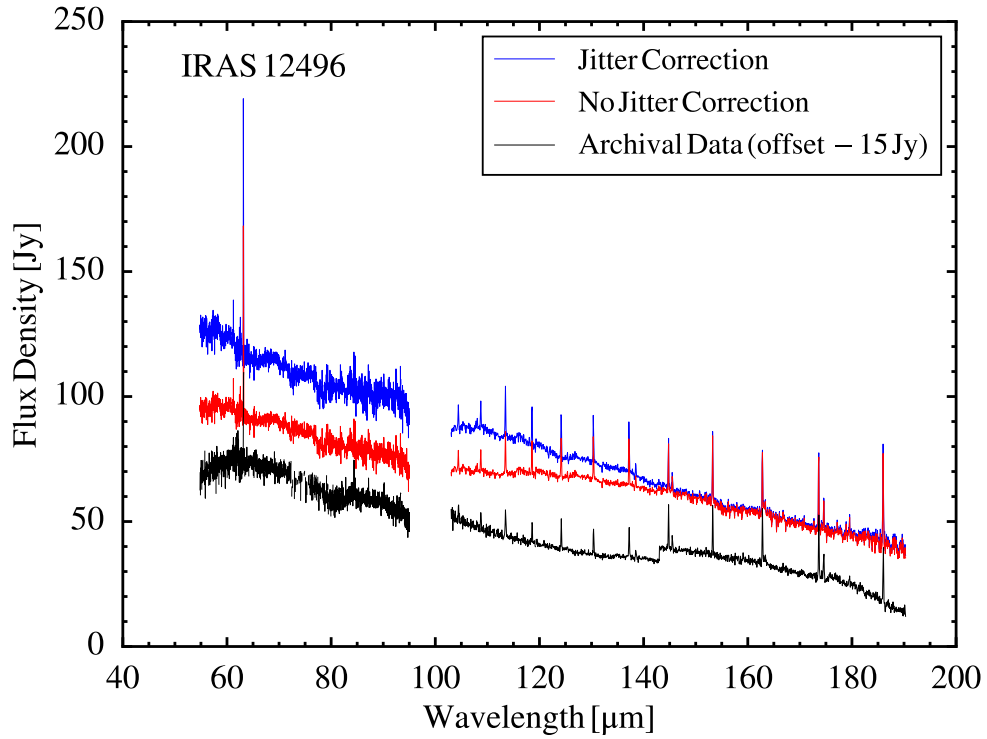


FIG. 2.—: The comparison of spectra of IRAS 12496 with different corrections applied. The archival data from HSA processed with the default pipeline are shown in black, offset by -15 Jy to separate it from the others. The offsets between modules and the incorrect shape at long wavelengths make searches for broad solid-state features impossible. Our reduction without jitter correction is shown in red; it improves the long wavelength behavior and module matching, but the no-jitter corrected spectrum shows a flattening around $130 \mu\text{m}$ that could be mistaken for a solid-state feature. The blue curve shows the result after jitter correction; the broad feature around $130 \mu\text{m}$ has been eliminated.

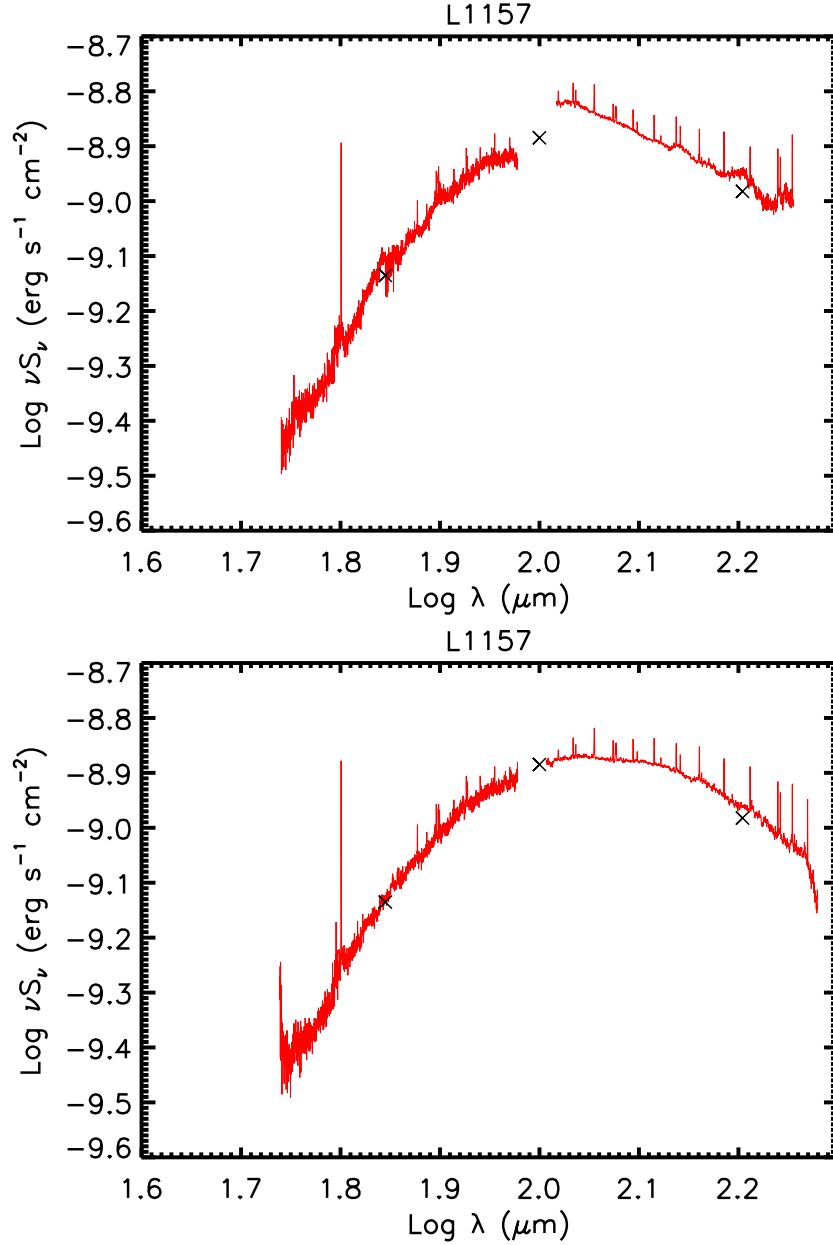


FIG. 3.— Improvement in data quality using new techniques, illustrated for L1157. The top plot shows the old (i.e. the 2012-13 era pipeline and calibration, without jitter correction and flatfielding correction) reduction without scaling. Photometric data (labeled by \times symbols) obtained later shows a substantial discrepancy. The bottom plot shows the results of the new reduction which produces smoother spectra and better agreement with photometry, without applied scaling. The flatfield corrections have also removed most of the false “solid-state features.” Note that published spectra from 2012-13 typically have scaling applied in post-processing.

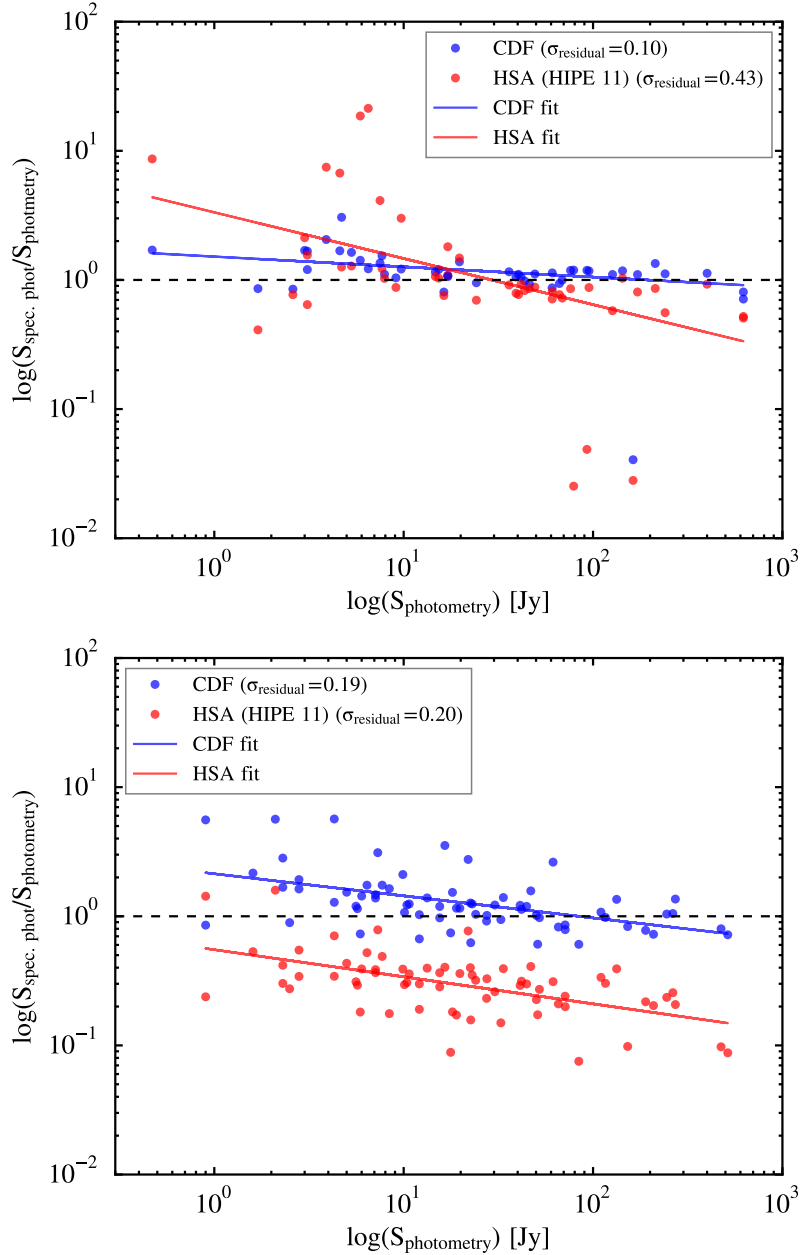


FIG. 4.— Comparison of spectral flux density with photometric flux density, for both the COPS-DIGIT-FOOSH archive and *Herschel* Science Archive (HSA) products. For PACS, shown in the top figure, data are collected from $\sim 1/3$ of total sources in our archive – all non-confused protostars for which we have gathered photometry data. For SPIRE, shown in the bottom figure, data are collected from 21 sources among 31 COPS sources for which we have gathered photometry data. Data from our archive are shown in blue, while data from the HSA are shown in red. The data from the HSA were processed in the HIPE 11 pipeline and collected in mid-2014. The σ parameter presented in the box is a measure of the deviation from the line of equality, normalized to the mean flux density. Spectra in our archive agree better with the photometric data, while the spectra from the HSA show larger deviations. The blue line is a fit to the data from the CDF archive only; the red line is a fit to the HSA data only. The significant outlier at the bottom right corner is excluded in this fitting. For both PACS and SPIRE, the CDF results are consistent with the equality line, while the HSA archive products are not.

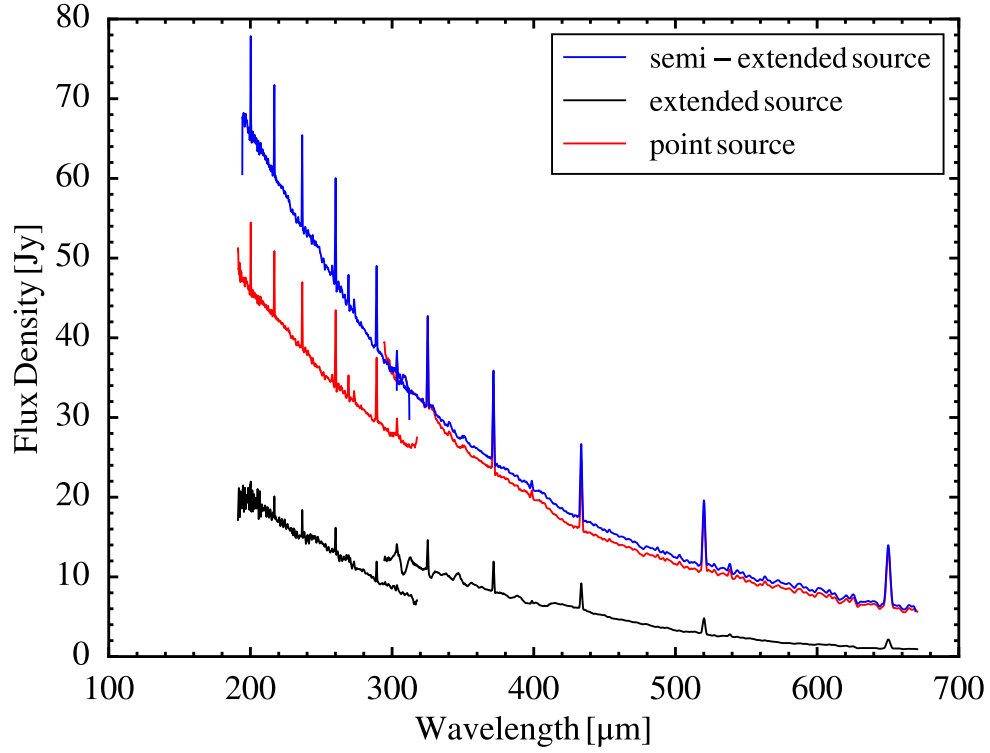


FIG. 5.—: Comparison of L1157 SPIRE spectroscopy calibrated with different correction methods: extraction as a point source (red), an extended source (black), and after the semi-extended source correction (blue).

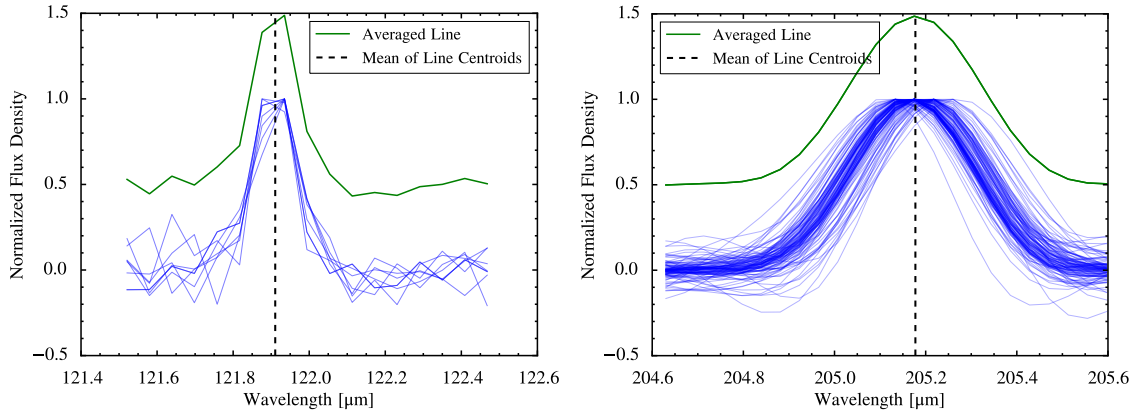


FIG. 6.—: The line profiles of [N II] 122 μm and [N II] 205 μm lines identified in this archive with SNR greater than 10. The individual line profiles are shown in blue, while the averaged line profile is shown in green. The line centroids of the averaged line profiles are reported in Table 6.

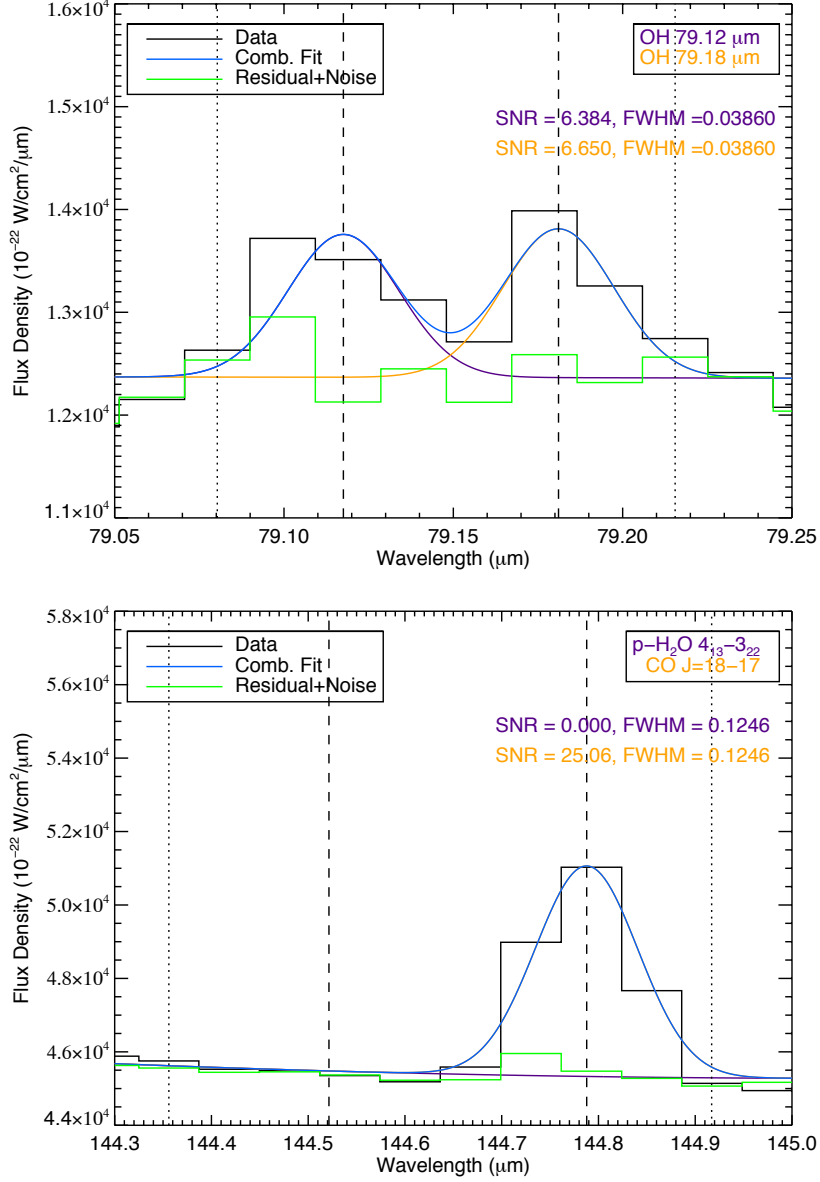


FIG. 7.—: Examples of double-gaussian fitting. **Top:** For the blended OH ${}^2\Pi_{1/2, 1/2}^- - {}^2\Pi_{3/2, 3/2}^+$ line and the OH ${}^2\Pi_{1/2, 1/2}^+ - {}^2\Pi_{3/2, 3/2}^-$ line, for L1157, using fixed line centroids and FWHM constraints. The lines plotted are data (black), combined fit (blue), OH ${}^2\Pi_{1/2, 1/2}^- - {}^2\Pi_{3/2, 3/2}^+$ fit (purple), OH ${}^2\Pi_{1/2, 1/2}^+ - {}^2\Pi_{3/2, 3/2}^-$ fit (yellow), and residual (green) (See §4.5). The SNR of the two OH lines are 6.38 and 6.65, respectively. Both lines are considered as detections. **Bottom:** An example of a double fit in which only a single component was detected. We show the blended p-H₂O 4₁₃-3₂₂ and CO $J = 18 \rightarrow 17$ lines, for BHR71, using fixed line centroids and FWHM constraints. The color code is the same as the top figure. The SNR of the CO line is 25 and is significant; the p-H₂O line is not detected.

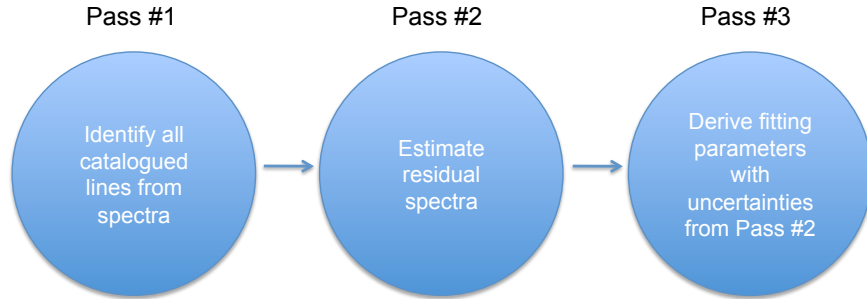


FIG. 8.— Summary of the three passes to fit spectral lines from an input 1-D spectrum.

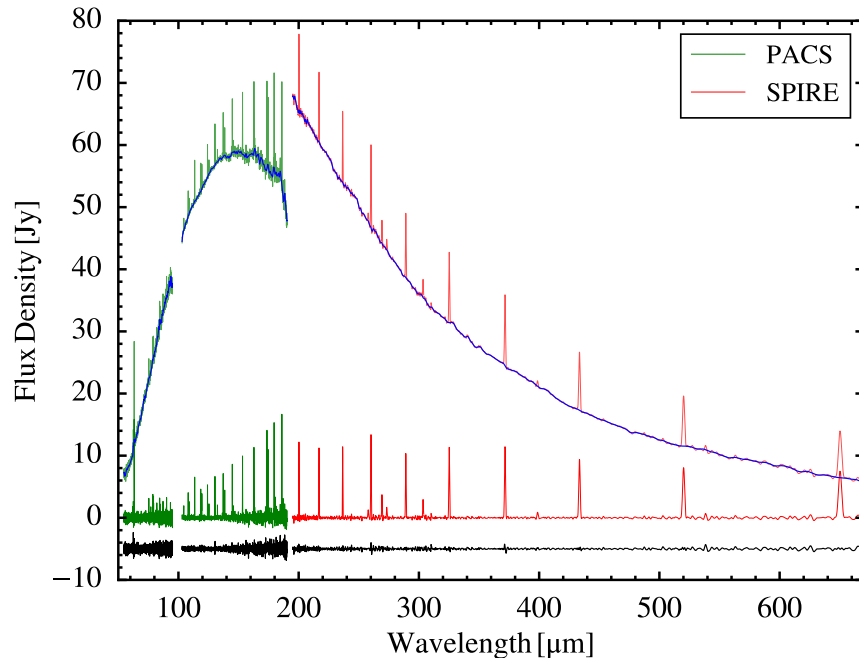


FIG. 9.— The spectrum of L1157 with flat spectrum (green/red for PACS/SPIRE, respectively), continuum (blue), and residual (black, offset by -5 Jy) overplotted. The continuum is the result of the smoothing function applied to the line-subtracted spectrum. The flat spectrum is produced by removing the continuum from the original spectrum. The residual spectrum is resulted from subtracting the continuum and fitted lines from the original spectrum. The comparison of the continuum and the flat spectrum at the edge of the PACS band shows that the fitting algorithm works well even in the region with severe instrumental effects. The offset between PACS and SPIRE spectra is discussed in Section 3.2.

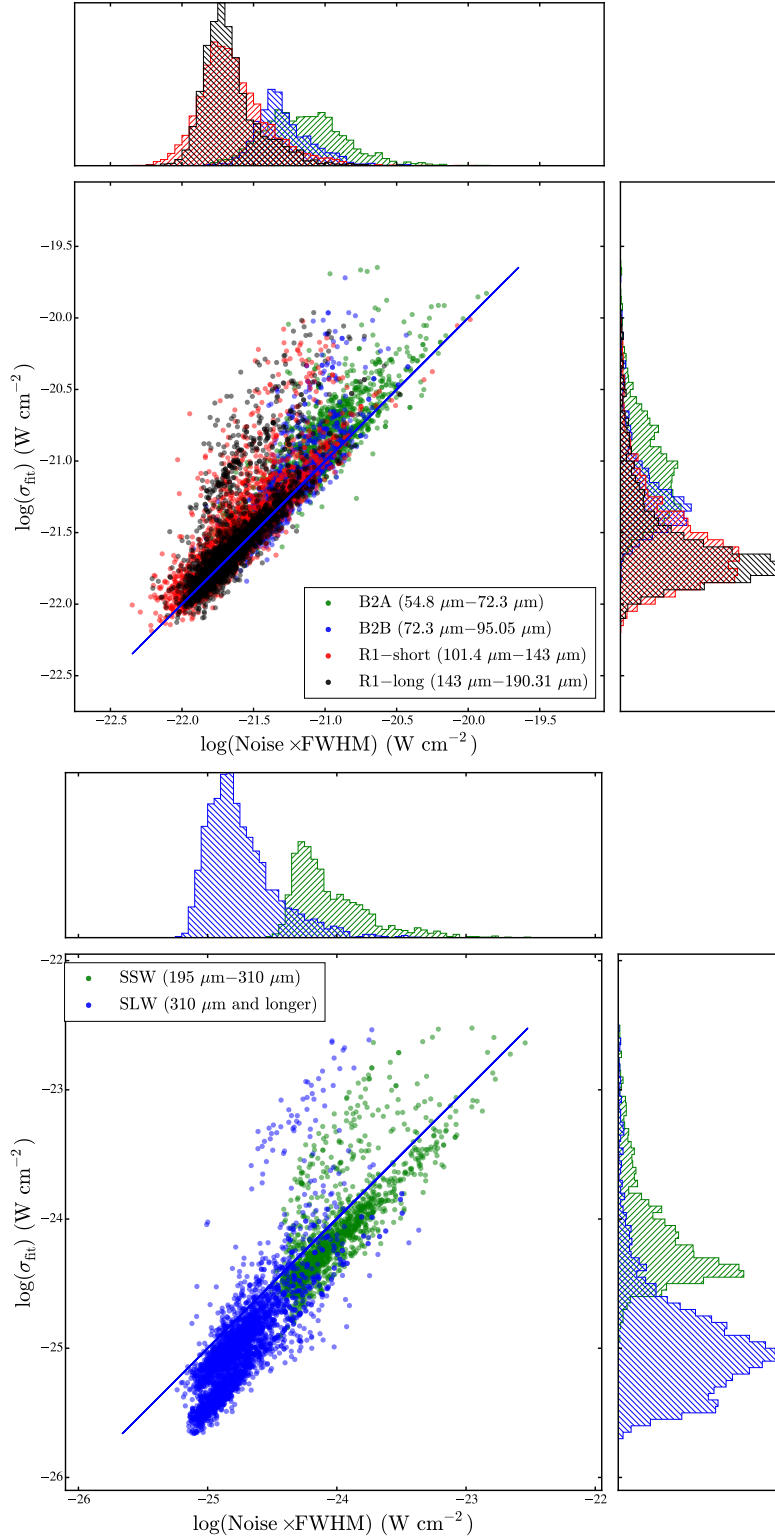


FIG. 10.—: The correlations of the uncertainties measured from the baseline and the uncertainties of the fitted parameters (Top: PACS, Bottom: SPIRE). Detections with different modules are presented in different colors (see legends). The blue line indicates the equality of two quantities with zero offset.

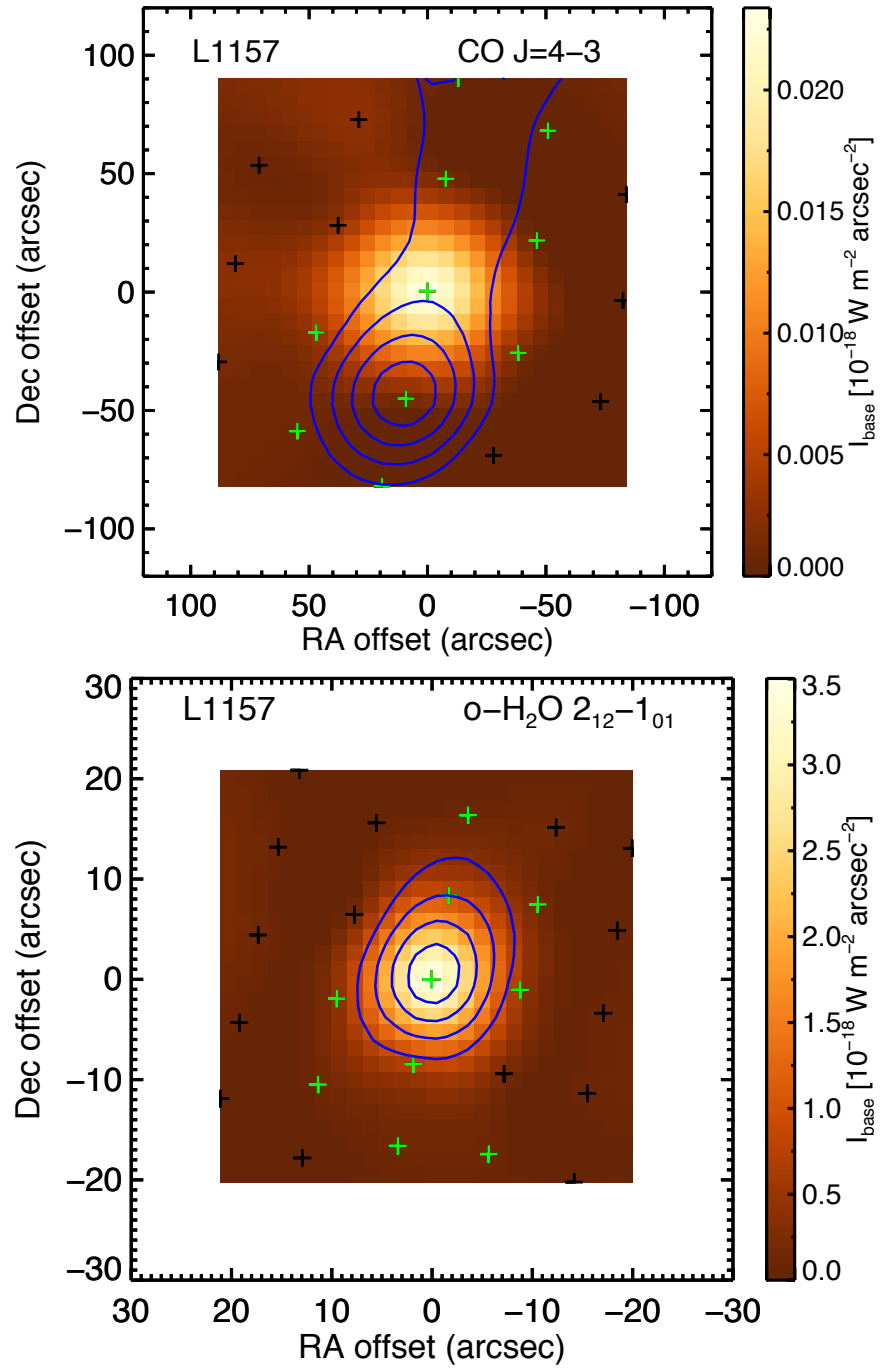


FIG. 11.—: An example of 2-D contour maps of L1157 CO $J = 4 \rightarrow 3$ and o-H₂O 2₁₂ – 1₀₁ line emission (blue contours) with local continuum (filled background) observed in SPIRE and PACS respectively. The green crosses indicate the spaxels that have detections.

5. Archive Structure and File Format

The archive can be accessed through the Herschel Science Archive under User Provided Data Products³ or as a downloadable archive file⁴. The file and directory trees contained in the archive are indicated in Figure 12. We provide the high-level data from the optimized pipeline and the products of line fitting results. The following section describes the file structure and how to interpret the individual formats.

5.1. File Structure

The schematic view of the file structure is shown in Figure 12. If there is no PACS or SPIRE observation available for a target, then the corresponding directory is not present. The detailed description of each product is described below. The products are identified in Figure 12 with the same letter (a through e) used to identify the following sections.

5.2. File Format

(a) 2-D reduced datacubes (FITS)

- PACS

We generate three datacubes for PACS in FITS format: Source–Nod A; Source–Nod B; Average (Source–(Nod A+Nod B) / 2). These can be read as dataplanes for each spaxel, with appropriate RA/Dec, and flux vs. wavelength. They are generated with wavelength grid oversample = 2 and upsample = 1 by default. These cubes include all corrections (in particular jitter correction).

Filename:

```
OBSID_1342xxxxxx.Targetname_blue/red_rebinnedcubesnoda_os#sf#.fits  
OBSID_1342xxxxxx.Targetname_blue/red_rebinnedcubesnodb_os#sf#.fits  
OBSID_1342xxxxxx.Targetname_blue/red_finalcubes_os#sf#.fits
```

We also generate these same three cubes *without* the pointing offset correction, with the addition of “_nojitter.fits” to the filename. We include the offset-corrected product only if the correction was successful. We include the non-offset corrected version for *all* sources. *If a jitter-corrected version is supplied, it means that we recommend using it.*

- SPIRE

We generate one datacube for SPIRE in FITS format. These can be read as dataplanes

³<http://www.cosmos.esa.int/web/herschel/user-provided-data-products>

⁴ftp://hsa.esac.esa.int/URD_rep/DIGIT/

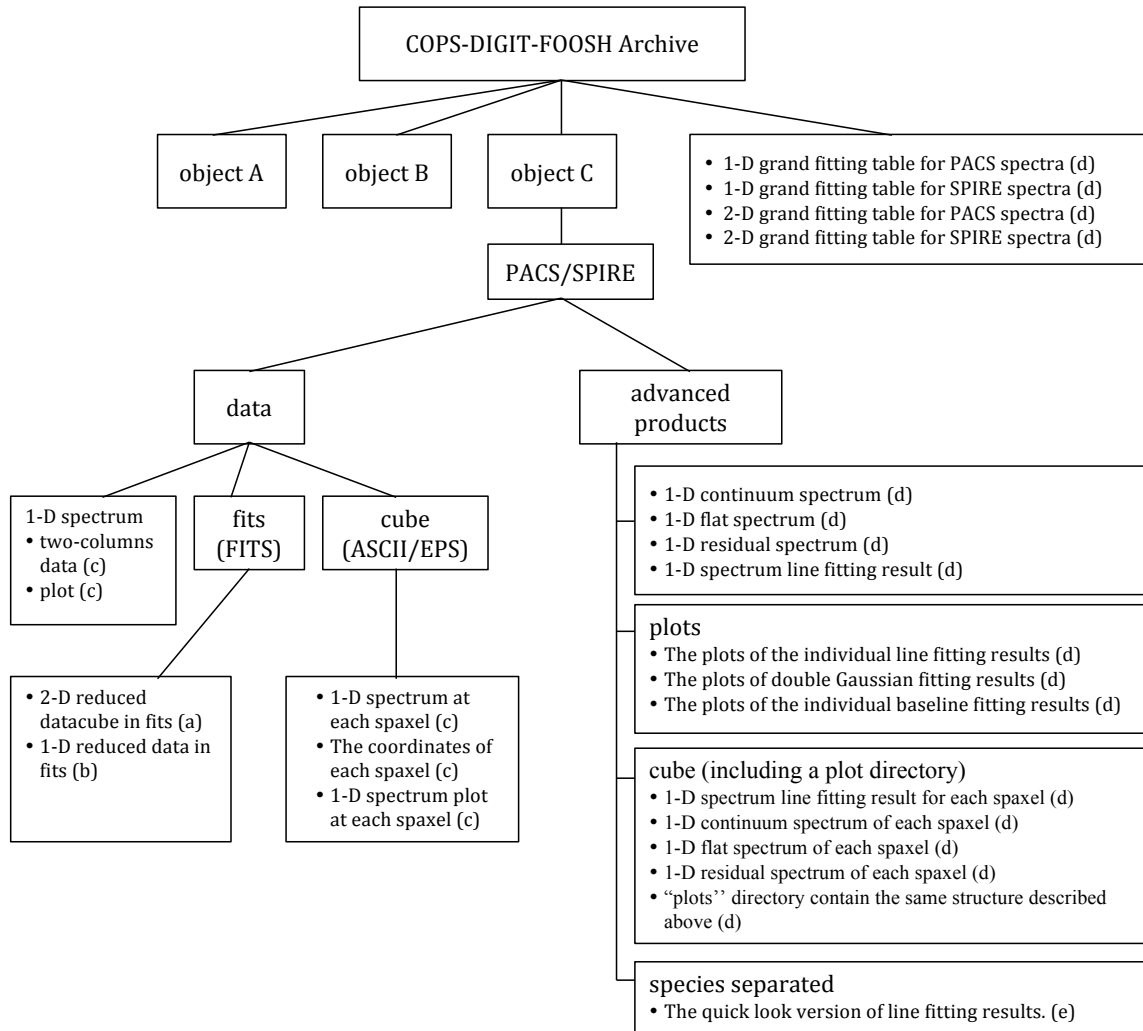


FIG. 12.—: The hierarchy structure of the archival file system. Files are organized primarily by the targets, and every target directory has the same substructure. The PACS and SPIRE high-level data and fitting results are stored in separate directories with the same structure. The letters refer to the sub-headings describing the products in §5.2.

for each spaxel, with appropriate RA/Dec, and flux vs. wavelength. Note that both SLW and SSW modules are included in a single FITS file. These cubes include all corrections.
Filename:

```
1342xxxxxx_spectrum_extended_HR_aNB_15.fits
```

There is no offset-corrected product being generated for SPIRE data.

(b) 1-D reduced spectra (FITS)

- PACS

We generate FITS files for three cases listed below, each with and without jitter correction; all six resulting files have the point source (PSF) correction applied. We also provide files in ASCII and EPS formats (see next section).

Filename:

```
OBSID_1342xxxxxx_Targetname_blue/red_centralSpaxel_  
PointSourceCorrected_Corrected3x3NO_slice00_os#sf#.fits
```

This is the simplest product, which is just the spectrum of the central spaxel with only the PSF correction applied. The “slice” is only non-zero for multiple rangescan or linescan observations, representing different wavelength settings within the original OBSID.

Filename:

```
OBSID_1342xxxxxx_Targetname_blue/red_centralSpaxel_  
PointSourceCorrected_Corrected3x3YES_slice00_os#sf#.fits
```

This is the same as the above product but with the jitter/pointing correction for the loss of light between pixels included in addition to the PSF correction. That is, we start with the central spaxel, and apply both the PSF and pointing/jitter correction.

We also generate the straight sum of the 3x3 spaxels, including PSF and pointing/jitter corrections:

Filename:

```
OBSID_1342xxxxxx_Targetname_blue/red_central9Spaxels_  
PointSourceCorrected_slice00_os#sf#.fits
```

A summation of the central 9 spaxels (the “3x3” case) with PSF correction applied.

So in summary, all three files have the point source (PSF) correction applied. The “3x3NO” is just this raw product. The “3x3YES” is the flux of the central spaxel after correcting for the PSF and the pointing/jitter. The “central9Spaxels” is the sum of the flux in the central 3x3 spaxels, still including the PSF/pointing jitter corrections.

We also output a version of these files without the pointing/jitter corrections. The filename is similar to the previous version, but with “_nojitter.fits” appended; “nojitter” refers to no jitter corrections applied.

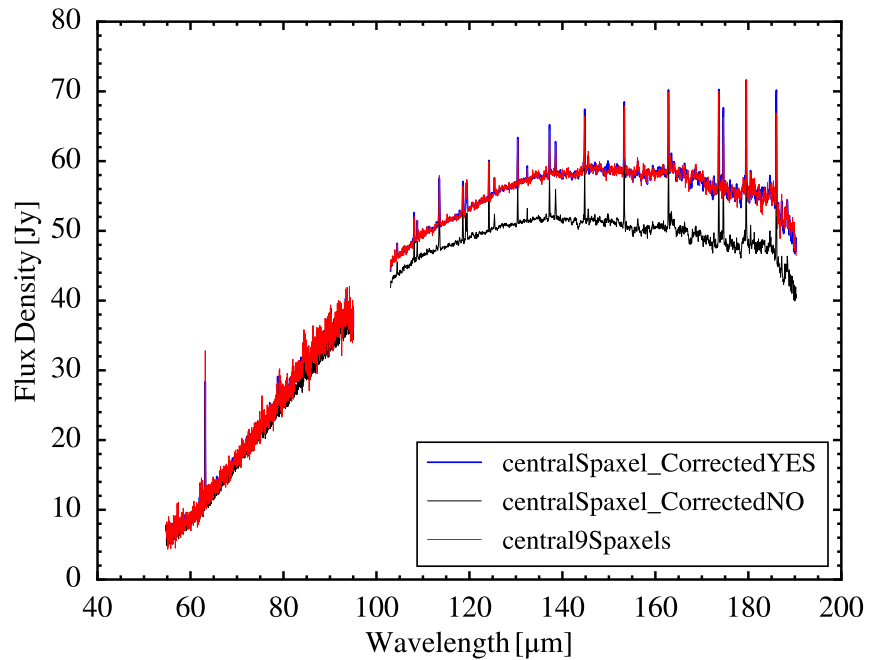


FIG. 13.—: Plot of our three PACS pipeline products, for protostar L1157. The blue spectrum shows the central spaxel product, with best SNR without accounting for source extent. The red spectrum is the sum of the central 9 spaxels in the PACS array; this likely includes all of the source flux, but also added noise from low SNR spaxels. The black spectrum is the best compromise product, flux calibrated to the red spectrum that has most of the source flux, but with SNR consistent with the blue spectrum. Note that lines are stronger in black than red with only modest increase of noise, therefore higher SNR.

We compare the three products for the case of L1157 in Figure 13. The blue spectrum shows the centralSpaxel product without the absolute flux calibration of the 3x3 aperture extraction; the red spectrum is the straight sum of the central 3x3 spaxels, and the black spectrum is the best product, combining the SNR of the central spaxel with the absolute flux calibration of the 3x3 aperture extraction.

- SPIRE

We generate one FITS file containing the SPIRE 1-D spectrum for each target. The spectra are processed by the pipeline setting described in §3.2 including “SemiExtendedSourceCorrector” routine.

Filename:

```
Targetname_spire_corrected.fits
```

In this FITS file, all of the dataplanes are ordered as in the 2-D datacube. But only dataplanes 5 and 8 containing the central spaxel in SLW and SSW are the ones with corrected values. The lines are fitted from these spectra as well.

(c) 1-D reduced spectra (two-columns ASCII/EPS)

For both the 1-D reduced spectra and 2-D datacubes, we extract the information (wavelength and flux) from the FITS files and report them in two-column ASCII format with plots of the corresponding spectrum for each spaxel or source. The same plotting method is applied to both 1-D spectra and spaxels within the datacubes. In PACS, we combine all of the modules (B2A, B2B and R1, see §2) together in ASCII files and plots. In addition, because the pointing coordinate of each spaxel varied slightly with wavelength, the files ending with “coord” contain the coordinates (RA/Dec) of each spaxel at each wavelength point. The coordinates reported in the 1-D spectra fitting results table are derived from the mean values of the coordinates across all wavelengths. The standard deviations of the coordinates across all wavelengths range from from 0.0073'' to 0.354'' for RA, and 0.0233'' to 0.4386'' for Dec. The mean values of the standard deviation are 0.129'' and 0.0675'' in RA and Dec respectively. But different modules are reported separately for SPIRE due to their different spaxel configurations. **We recommend using the coordinates from the files we provided instead of reading in from the header of the FITS files.**

Filename:

(1-D)

```
Targetname_reduction_trim.txt
```

```
Targetname_reduction_trim.eps
```

(2-D)

```
Targetname_pacs_pixel##_os#sf#.txt
```

```
Targetname_pacs_pixel##_os#sf#_coord.txt
```

```
Targetname_pacs_pixel##_os#sf#.eps
```

```
Targetname_pixelname.txt
```

Targetname_pixelname.eps

These ASCII files (and the corresponding EPS plots) are trimmed consistently at specific wavelengths. Here we describe trimming details for PACS and SPIRE separately.

- PACS

For the shortest wavelength module (B2A), we remove all wavelengths short of $54.80 \mu\text{m}$, and long of $72.3 \mu\text{m}$. For the next shortest (B2B), we trim all wavelengths short of $72.3 \mu\text{m}$ and long of $95.05 \mu\text{m}$. For the third (R1; 100-145 μm), we remove all wavelengths short of $101.4 \mu\text{m}$ and long of $143.0 \mu\text{m}$. For the fourth (R1; 145-210 μm), we trim all wavelengths short of $190.31 \mu\text{m}$ and long of $143.0 \mu\text{m}$.

- SPIRE

For the shorter wavelength module (SSW), we remove all wavelengths short of $195 \mu\text{m}$ and long of $310 \mu\text{m}$. For the longer wavelength module (SLW), we remove all wavelengths short of $310 \mu\text{m}$.

We find this method gives the best overall continuum fit between modules, with the highest SNR and consistent continuum in the overlap regions, stitched into a single 1-D spectrum. Figure 14 shows the original spectra from all modules, and the shaded regions indicate the part preserved after the trimming. The regions where the continuum behaves abnormally and/or the noise increases significantly are excluded via the trimming process. Note that the original, untrimmed spectra are still present in our archive. The FITS files previously described do not use these trim points and present the full spectra from all modules. An example of the final trimmed spectra of the protostar L1157 (PACS and SPIRE) is shown in Figure 15, with each module highlighted by color.

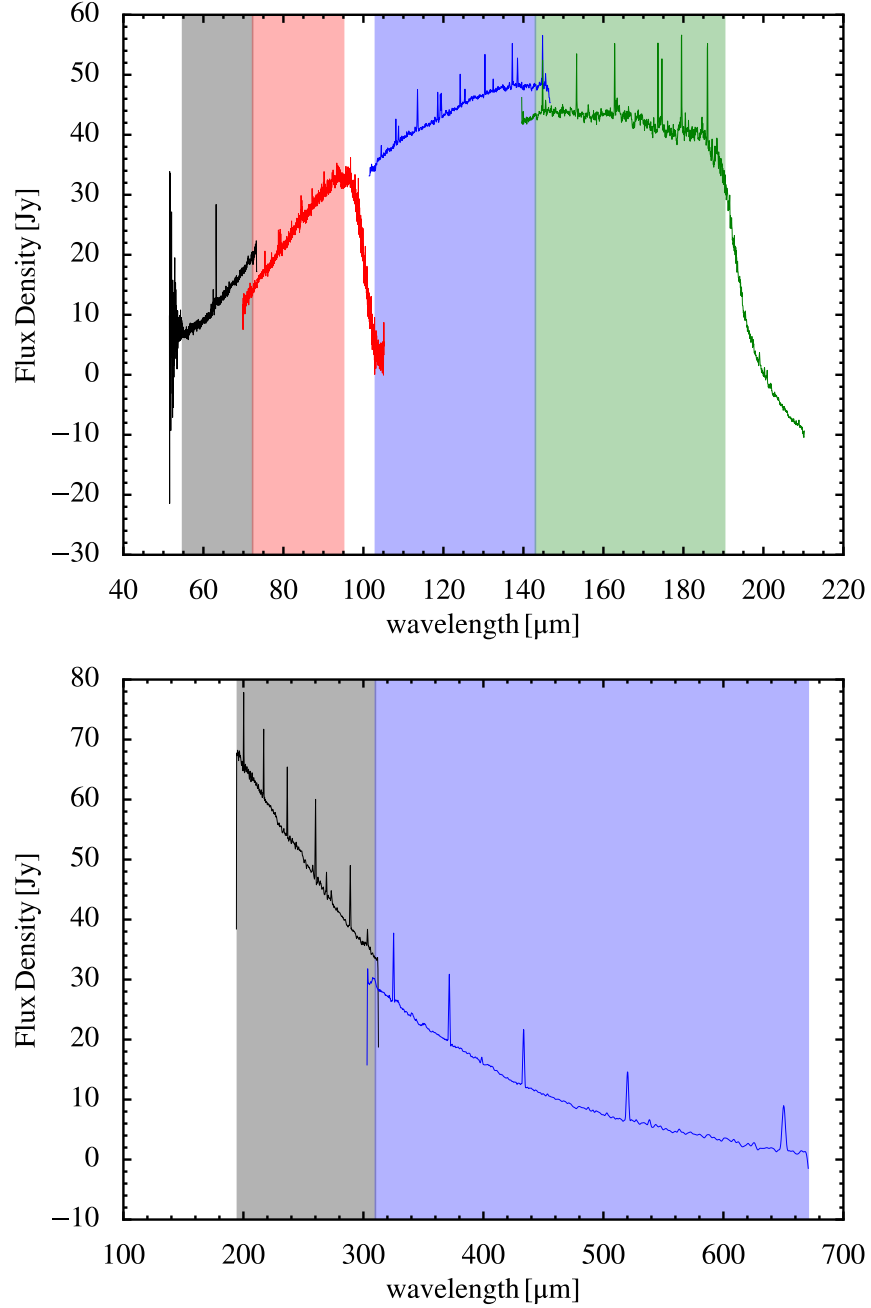


FIG. 14.—: Original spectra of L1157, each module shown in a different color. The PACS spectra are shown at the top, while the SPIRE spectra are shown at the bottom. Note that the PACS spectra are shifted by -5 Jy between each module and the SPIRE spectra are shifted by 5 Jy between two modules for better visualization of the overlap regions. The shaded area indicates the region where the spectrum with the same color is preserved after trimming.

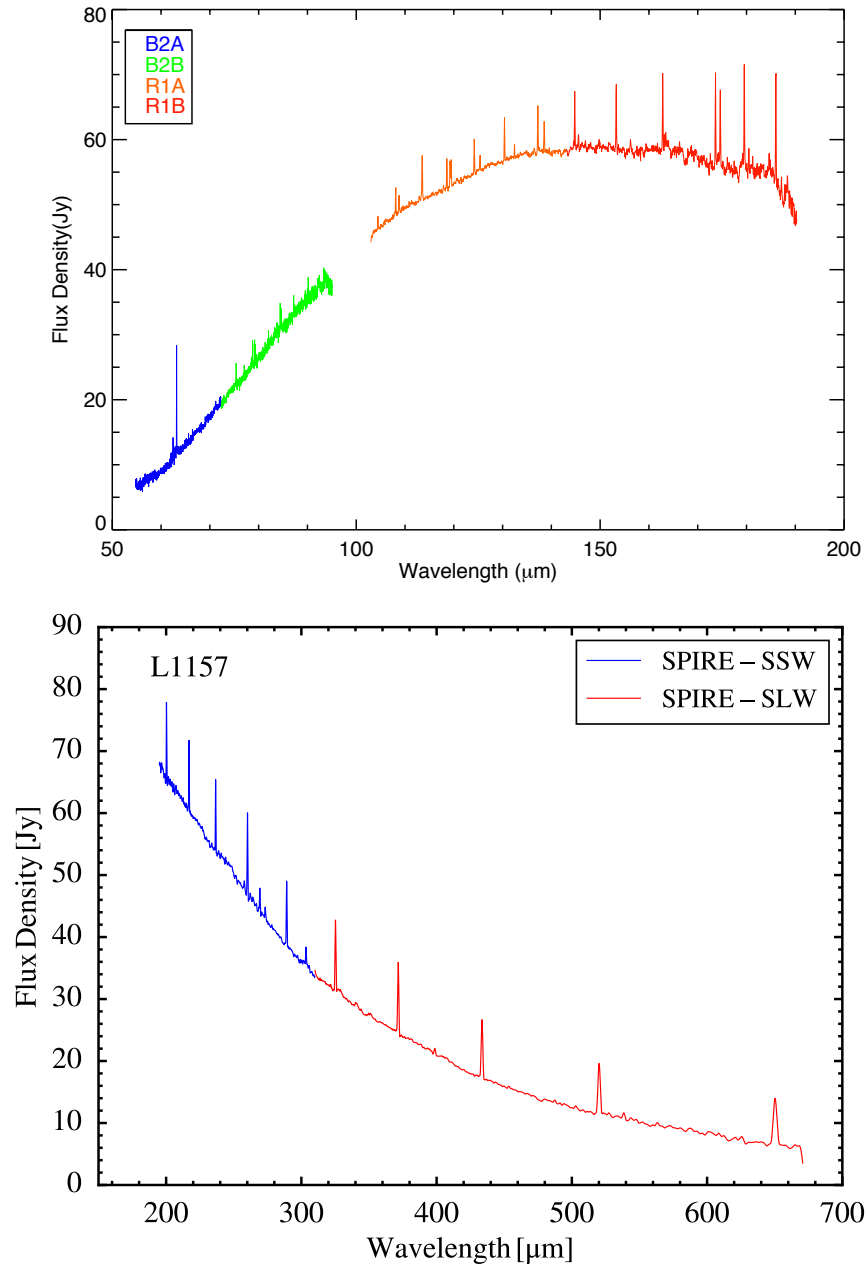


FIG. 15.— **Top:** An example 1-D PACS spectrum of L1157, with the four modules highlighted by color. **Bottom:** An example 1-D SPIRE spectrum of L1157, with the two modules highlighted by color.

(d) Line fitting results

The line fitting results are reported in text and figures format. The ASCII files provide the tables of the fitting results so that users can read them in with any language they prefer. The figures visualize the fitting results with the original data, fitted line(s), and residual. The users can visually check the fitting results with the figures easily.

Filename:

(PACS)

```
Targetname_reduction_trim_lines.txt
Targetname_reduction_trim_continuum.txt
Targetname_reduction_trim_flat_spectrum.txt
Targetname_reduction_trim_residual_spectrum.txt
Targetname_pacs_pixel##_os#sf#_lines.txt
Targetname_pacs_pixel##_os#sf#_continuum.txt
Targetname_pacs_pixel##_os#sf#_flat_spectrum.txt
Targetname_pacs_pixel##_os#sf#_residual_spectrum.txt
```

(SPIRE)

```
Targetname_spire_corrected_lines.txt
Targetname_spire_corrected_continuum.txt
Targetname_spire_corrected_flat_spectrum.txt
Targetname_spire_corrected_residual_spectrum.txt
Targetname_pixelname_lines.txt
Targetname_pixelname_continuum.txt
Targetname_pixelname_flat_spectrum.txt
Targetname_pixelname_redsidual_spectrum.txt
```

The ASCII format line fitting results are presented in four output forms (lines, continuum, flat_spectrum, and noise_spectrum), as listed above. The first contains the full report of the line fitting results using the method described in §4, containing the fitted line parameters (Table 8) of each line in the full input list – including non-detections. Users can simply read this report and apply the fitting results. The second file contains the continuum spectrum of the source produced by subtracting the fitted lines from the original spectrum. The third file is the counterpart of the continuum file, a continuum-subtracted spectrum in which only the spectral lines and flat baseline remain (Figure 9). The fourth file contains the residual spectrum after the subtraction of fitted lines and smoothed continuum. The file names of PACS spectra are listed in the first block with the first four as the products of 1-D spectra and last four as the products of 2-D spectra, while file names of SPIRE spectra are listed in the second block with the same fashion.

(Fitting table including all sources)
CDF_archive_pacs_1d_lines.txt
CDF_archive_pacs_cube_lines.txt
CDF_archive_spire_1d_lines.txt
CDF_archive_spire_cube_lines.txt

The fitting results of 1-D PACS, 1-D SPIRE, 2-D PACS, and 2-D SPIRE of all sources are stored in separate ASCII files with similar tables to those described above and in §4 with an additional column with the object name, and a summary table that includes ALL fitting results (PACS, SPIRE, 1-D, and 2-D) is provided with a name of CDF_archive_lines.txt, in which the pixel column is labeled as ``c`` for 1-D spectra.

(Individual line fitting plot in PACS)
spectrum_line_subtracted.Targetname_reduction_trim.eps
Targetname_reduction_trim_linename.eps
Targetname_reduction_trim_line1+line2.eps (in ``double_gauss`` folder)

(Individual line fitting plot in SPIRE)
Targetname_spectrum_line_subtracted_spire_corrected.eps
Targetname_spire_corrected_linename.eps
Targetname_spire_corrected_line1+line2.eps (in ``double_gauss`` folder)

The figures are all presented for typical spectra with various levels of data, as listed above. The first three of the six items are figures for PACS, while the last three of six are for SPIRE. The files with “spectrum_line_subtracted” provide overviews for line fitting results of each object and each instrument. It includes the original data (black), continuum (blue), and residual spectrum (green). The files with “linename” provide the visualization of the fitting result for each line (Figure 16 top). It includes original data (black), fitted line (blue), and residual/noise (green). The vertical lines represent the allowed region for line (dash line) and the region taken for the baseline fitting (dotted line). And the SNR and FWHM are printed within the figures. The fitting results of the double Gaussian, stored in ``double_gauss`` folder, are plotted in figures with two lines in their file names (“line1+line2”) with an additional fitted line in orange (Figure 7). We also report the fitting results of the baseline in the subdirectory named “base” (Figure 16 bottom). The plot includes the original data (black), the fitted baseline (purple), residual (red), and the points taken in the baseline fitting (asterisks). There is another directory named “cannot_fit” which includes the very rare case when the fitting failed to coverage.

(e) Quick look output for the fitting results

Filename:
Targetname_reduction_trim_lines_species.txt
Targetname_spire_corrected_species.txt

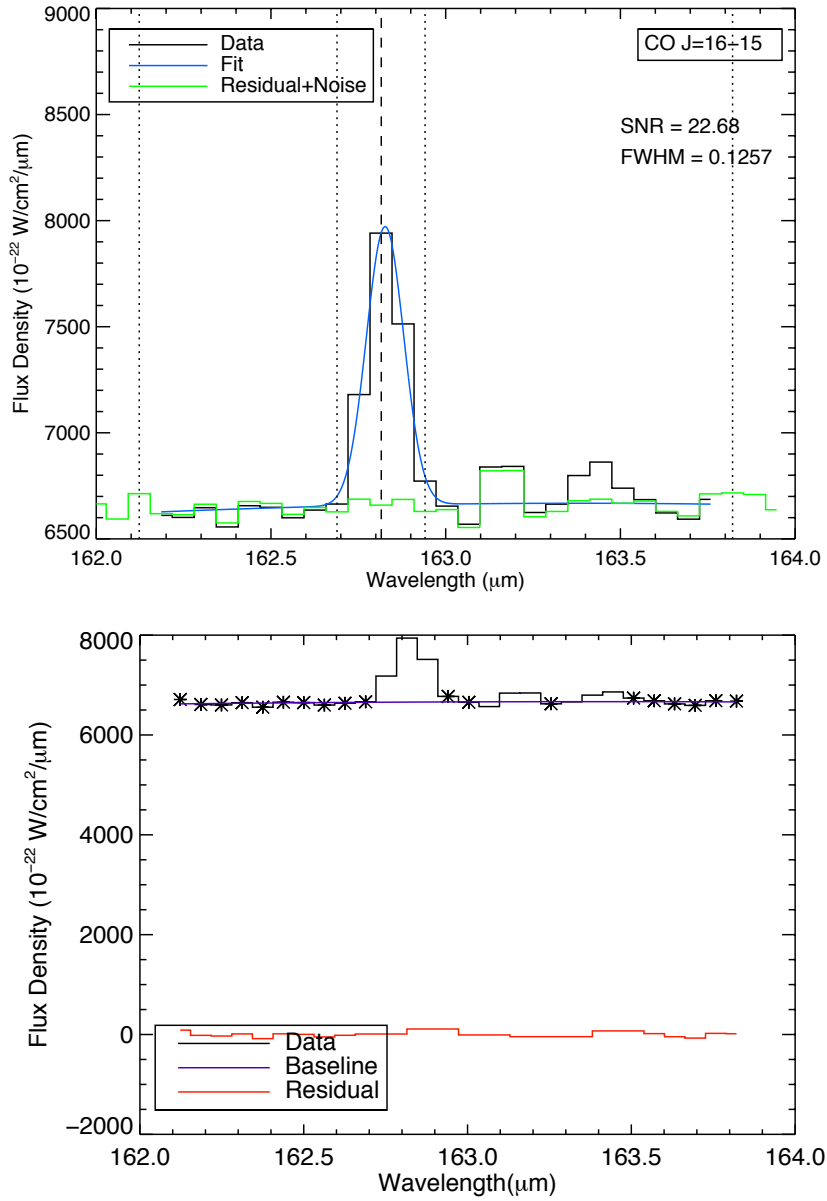


FIG. 16.—: **Top:** An example of single line fitting result of CO $J = 16 \rightarrow 15$ in L1157. **Bottom:** An example of the baseline fitting result at the region of CO $J = 16 \rightarrow 15$ in L1157. The asterisks indicate the points used for the baseline fitting.

This output provides the user a convenient quick look at the source spectral properties and evaluation of the fitting quality. These files contain the sorted line information of either the 1-D spectrum or the spectrum of each spaxel for given molecular/atomic species. The line profiles of seven different species are separated including CO, ^{13}CO , HCO^+ , OH, o- H_2O , p- H_2O , and atomic fine-structure transitions. The data for each molecule are stored in the corresponding files.

5.3. Comparison to Previously Published Results

The scientific implications of the reprocessed data archive will be reported in other papers. We note here the impact of the new archive on rotational temperatures and densities reported in [Green et al. \(2013a\)](#) and other works. We compared a sample of 18 sources with measured (PACS only) rotational temperatures and densities, divided into “warm” (~ 300 K) and “hot” (~ 1000 K) components as defined in previous papers, measured using the 2012-13 pipeline and again with the current pipeline. The rotational temperatures changed insignificantly: the average warm component temperature increased by 1.4% (ranging between -18% and 25%), while the average hot component temperature decreased by 1.5% (almost entirely due to one source, GSS30-IRS1, decreasing by 7%). In contrast, the derived number densities were altered substantially. The average warm component increased in count by 17.6% (ranging from -27.5% to 62.5%, with outlier GSS30-IRS1 increasing by 198%). The hot component increased by 22%, but this was entirely because of GSS30-IRS1, which increased 107%; with that source omitted, the mean of the rest changed by less than 2%.

Thus the measured temperature values have changed only minimally, and the hot component was only slightly different except in cases where we properly captured the extended nature of the source in the new data products. In GSS30-IRS1 in particular, we previously used the central spaxel only, and did not include extended emission; in this new analysis, we include the larger region. However, we do not attempt to disentangle GSS30, as was done using earlier data products; [Je et al. \(2015\)](#) deconvolved GSS30 into three separate IR sources. However, the increase in the warm component molecule number count is widespread in our sample, and is due to the calibration improvements in the long wavelengths of the PACS pipeline (100-190 μm).

In general, the adjustment in line flux does not impact previous results qualitatively. [Green et al. \(2013a\)](#) noted in Figure 23 that the low density solution in [Neufeld \(2012\)](#) was a good fit to the CO rotational diagram for B335; this conclusion is unchanged.

[Lindberg et al. \(2014\)](#) and [Dionatos et al. \(2013\)](#) considered complicated regions (RCrA and Serpens, respectively) and created prescriptions to deconvolve the sources therein. Our pipeline does not consider the deconvolution problem and we recommend using the earlier works. For example, [Dionatos et al. \(2013\)](#) find that the lines peak at the position of outflow shocks rather than the protostellar sources. This can be identified from the contour plots in our dataset, and would require custom extraction techniques. We provide a well-calibrated spectrum for Serpens-SMM3 including

the jitter correction; however the complex of shocks causes a different distribution of lines. Serpens-SMM4 was not successfully corrected for pointing jitter as noted in Table 1. Similarly, RCrA-IRS7B is calibrated via our pipeline, but RCrA-IRS7C is not successfully corrected. In each case, the earlier work uses line fluxes from spaxels associated with outflow shocks rather than the continuum (protostellar) sources. Both find that the rotational temperatures of the spaxels dominated by shocks are similar to those toward the protostar, but the number of molecules is different. In each case, we expect that using our new dataset would provide reduced absolute calibration and line flux uncertainty, but the deconvolution would still be required as post-processing.

The case of L1448-MM (Lee et al. 2013) is similar, but the central source dominates the continuum and line fluxes. Thus the deconvolution is required to separate L1448-C, N, and S, but the overall results for the dominant submillimeter source L1448-MM are not significantly changed.

Finally, the FOOSH dataset included both an earlier SPIRE and PACS reduction, and 4 of those objects appear in this dataset. The warm (PACS) component was only detected in V1057 Cyg and the temperature has increased by a factor consistent with the DIGIT PACS sources, 17%, with a similar decrease in number, consistent with the spread in changes seen in the DIGIT sample. However, some of the SPIRE data are significantly changed. FU Ori still includes no significant CO detections in the SPIRE bands. V1057 Cyg exhibited a well-characterized cool component which was essentially unchanged ($\sim 3\%$). V1515 Cyg and V1331 Cyg had only 3 detections in the earlier work; V1331 Cyg now has 6 CO lines detected, and this has altered the rotational properties considerably. The cool CO rotational temperatures increased in both sources, from $\sim 20\text{-}30$ K to $75\text{-}100$ K, and the number of molecules dropped by a factor of 2. We conclude that the improvement in absolute flux calibration can dramatically change the number of molecules detected in the SPIRE bands, and the correction for extended sources can alter the temperature.

6. Conclusions

We have provided a dataset of *Herschel*-PACS and SPIRE spectroscopy to generate a broadly accessible archive with easily downloaded data products (grids of maps, continuum, lines, and full SEDs) of publishable quality. This dataset will complement and enhance the *Herschel* Science Archive, to serve the community with a Legacy Archive for young stellar objects. Expected legacy investigations will reveal fundamental constraints on accretion processes, environments of protostars, and the conditions in emerging protoplanetary disks.

JDG would like to acknowledge numerous helpful discussions with the PACS and SPIRE ICC teams, via webinars, helpdesk queries, and contacts. Support for this work, part of the *Herschel* Open Time Key Project Program, was provided by NASA through awards issued by the Jet Propulsion Laboratory, California Institute of Technology. J.-E.L. was supported by the 2013 Sabbatical Leave Program of Kyung Hee University (KHU-20131724) and also supported by Basic Science Research Program through the National Research Foundation of Korea(NRF) funded by the Ministry of Science, ICT and future Planning (2015R1A2A2A01004769). JDG and Y-LY acknowledge

support from NASA Herschel Science Center Cycle 2 grants. RL acknowledges support from the Karl G. Henize Endowed Scholarship, the John W. Cox Endowment for the Advanced Studies in Astronomy, and the College of Natural Sciences Summer Undergraduate Research Fellowship at the University of Texas at Austin. AK acknowledges support from the Foundation for Polish Science (FNP) and the Polish National Science Center grant 2013/11/N/ST9/00400.

REFERENCES

- Authier, N., Bagland, N., & Lefloch, A. 1993, *Journal of Molecular Spectroscopy*, 160, 590
- Balog, Z., Müller, T., Nielbock, M., et al. 2014, *Experimental Astronomy*, 37, 129
- Bendo, G. J., Griffin, M. J., Bock, J. J., et al. 2013, *MNRAS*, 433, 3062
- Ceccarelli, C., Caux, E., Loinard, L., et al. 1999, *A&A*, 342, L21
- Cieza, L. A., Olofsson, J., Harvey, P. M., et al. 2013, *ApJ*, 762, 100
- Dionatos, O., Jørgensen, J. K., Green, J. D., et al. 2013, *A&A*, 558, A88
- Dunham, M. M., Evans, N. J., Terebey, S., Dullemond, C. P., & Young, C. H. 2010, *ApJ*, 710, 470
- Dunham, M. M., Stutz, A. M., Allen, L. E., et al. 2014, arXiv:1401.1809
- Evans, N. J., Dunham, M. M., Jørgensen, J. K., et al. 2009, *ApJS*, 181, 321
- Flower, D. R. & Pineau Des Forêts, G. 2010, *MNRAS*, 406, 1745
- Giannini, T., Lorenzetti, D., Tommasi, E., et al. 1999, *A&A*, 346, 617
- Giannini, T., Nisini, B., & Lorenzetti, D. 2001, *ApJ*, 555, 40
- Goorvitch, D. 1994, *ApJS*, 95, 535
- Green, J. D., Evans, II, N. J., Jørgensen, J. K., et al. 2013a, *ApJ*, 770, 123
- Green, J. D., Evans, II, N. J., Kóspál, Á., et al. 2013b, *ApJ*, 772, 117
- Griffin, M. J., Abergel, A., Abreu, A., et al. 2010, *A&A*, 518, L3+
- Higdon, S. J. U., Devost, D., Higdon, J. L., et al. 2004, *PASP*, 116, 975
- Je, H., Lee, J.-E., Lee, S., Green, J. D., & Evans, N. J., II 2015, *ApJS*, 217, 6
- Karska, A., Herczeg, G. J., van Dishoeck, E. F., et al. 2013, *A&A*, 552, A141
- Kaufman, M. J. & Neufeld, D. A. 1996, *ApJ*, 456, 611
- Kim, H. J., Evans, II, N. J., Dunham, M. M., Lee, J.-E., & Pontoppidan, K. M. 2012, *ApJ*, 758, 38

Kristensen, L. E., van Dishoeck, E. F., Bergin, E. A., et al. 2012, *A&A*, 542, A8

Lahuis, F., Kessler-Silacci, J. E., Knez, C., et al. 2006, *c2d Spectroscopy Explanatory Supplement*.
(Pasadena, CA: Spitzer Science Center)

Lee, J., Lee, J.-E., Lee, S., et al. 2013, *ApJS*, 209, 4

Lindberg, J. E., Jørgensen, J. K., Green, J. D., et al. 2014, *A&A*, 565, A29

Lorenzetti, D., Giannini, T., Nisini, B., et al. 2000, *A&A*, 357, 1035

Lorenzetti, D., Tommasi, E., Giannini, T., et al. 1999, *A&A*, 346, 604

Markwardt, C. B. 2009, in *Astronomical Society of the Pacific Conference Series*, Vol. 411, *Astronomical Data Analysis Software and Systems XVIII*, ed. D. A. Bohlender, D. Durand, & P. Dowler, 251

Müller, H., Schlöder, F., Stutzki, J., & Winnewisser, G. 2005, *Journal of Molecular Structure*, 742, 215

Müller, T., Balog, Z., Nielbock, M., et al. 2014, *Experimental Astronomy*, 37, 253

Neufeld, D. A. 2012, *ApJ*, 749, 125

Nisini, B., Benedettini, M., Codella, C., et al. 2010, *A&A*, 518, L120

Nisini, B., Giannini, T., & Lorenzetti, D. 2002, *ApJ*, 574, 246

Offner, S. S. R. & McKee, C. F. 2011, *ApJ*, 736, 53

Palla, F. & Stahler, S. W. 1993, *ApJ*, 418, 414

Poglitsch, A., Waelkens, C., Geis, N., et al. 2010, *A&A*, 518, L2

Rebull, L. M., Padgett, D. L., McCabe, C.-E., et al. 2010, *ApJS*, 186, 259

Schöier, F. L., van der Tak, F. F. S., van Dishoeck, E. F., & Black, J. H. 2005, *A&A*, 432, 369

van Dishoeck, E. F., Kristensen, L. E., Benz, A. O., et al. 2011, *PASP*, 123, 138

Wampfler, S. F., Bruderer, S., Karska, A., et al. 2013, *A&A*, 552, A56

Ward-Thompson, D., André, P., Crutcher, R., et al. 2007, *Protostars and Planets V*, 33, arXiv:astro-ph/0603474

Yang, B., Stancil, P. C., Balakrishnan, N., & Forrey, R. C. 2010, *ApJ*, 718, 1062

Shirley, Y. L., Evans, N. J., II, Rawlings, J. M. C., & Gregersen, E. M. 2000, *ApJS*, 131, 249

Young, C. H., Bourke, T. L., Young, K. E., et al. 2006, *AJ*, 132, 1998

Wu, J., Dunham, M. M., Evans, N. J., II, Bourke, T. L., & Young, C. H. 2007, AJ, 133, 1560

Wu, R., Polehampton, E. T., Etxaluze, M., et al. 2013, A&A, 556, A116

7. Appendix: Sourcelist and Data Product Status

The comprehensive source list, OBSID number, RA, Dec, and reduction type are listed in Table 1.

Table 1:: Archive Sources

Source	Other Name	PACS SIDs	OB- OBSID	SPiRE	RA	Dec	Prog.	Jitter Corr.	SPiRE 1-D
AB Aur		1342217842, 1342217843			04h55m45.8s	+30d33m04.3s	D	x	
AS 205		1342215737, 1342215738			16h11m31.4s	-18d38m26s	D	x	
B1-a		1342216182, 1342216183	1342249475		03h33m16.7s	+31d07m55.2s	D,C	x	x
B1-c		1342216213, 1342216214	1342249476		03h33m17.9s	+31d09m31.9s	D,C	x	x
B335		1342208889, 1342208888	1342253652		19h37m00.9s	+07d34m09.7s	D,C	x	x
BHR 71		1342212230, 1342212231	1342248249		12h01m36.3s	-65d08m53.0s	D,C	x	x
Ced110-IRS4			1342248246		11h06m47.0s	-77d22m32.4s	C		x
DG Tau		1342225730, 1342225731			04h27m04.7s	+26d06m16s	D	x	
DK Cha	IRAS 12496-7650	1342188039, 1342188040	1342254037		12h53m17.2s	-77d07m10.7s	D,C	x	x
EC 82	[EC92] 82	1342192975, 1342219435			18h29m56.9s	+01d14m47s	D		
Elias 29		1342228519, 1342228520			16h27m09.4s	-24d37m18.6s	D	x	x
FU Ori		1342250907, 1342250908	1342230412		05h45m22.4s	+09d04m12s	F	x	x
GSS30-IRS1		1342215678, 1342215679	1342251286		16h26m21.4s	-24d23m04.3s	D,C	x	x
HD 100453		1342211695, 1342211696			11h33m05.6s	-54d19m29s	D	x	

Source	Other Name	PACS OBSIDs	SPIRE OBSID	RA	Dec	Prog.	Jitter Corr.	SPIRE 1-D
HD 100546		1342188037, 1342188038		11h33m25.4s	-70d11m41s	D	x	
HD 104237		1342207819, 1342207820		12h00m05.1s	-78d11m35s	D	x	
HD 135344		1342213921, 1342213922		15h15m49.0s	-37d08m56s	D	x	
HD 139614		1342215683, 1342215684		15h40m46.4s	-42d29m54s	D	x	
HD 141569		1342213913		15h49m57.8s	-03d55m16s	D	x	
HD 142527		1342216174, 1342216175		15h56m41.9s	-42d19m23s	D	x	
HD 142666		1342213916		15h56m40.0s	-22d01m40s	D		
HD 144432		1342213919		16h06m58.0s	-27d43m10s	D	x	
HD 144668		1342215641, 1342215642		16h08m34.3s	-39h06m18s	D	x	
HD 150193		1342227068		16h40m17.9s	-23d53m45s	D	x	
HD 163296		1342217819, 1342217820		17h56m21.3s	-21d57m22s	D	x	
HD 169142		1342206987, 1342206988		18h24m29.8s	-29d46m49s	D	x	
HD 179218		1342208884, 1342208885		19h11m11.3s	+15d47m16s	D	x	
HD 203024		1342206975		21h16m03.0s	+68d54m52s	D		
HD 245906		1342228528		05h39m30.5s	+26d19m55s	D		
HD 35187		1342217846		05h24m01.2s	+24d57m38s	D	x	
HD 36112		1342228247, 1342228248		05h30m27.5s	+25d19m57s	D	x	
HD 38120		1342226212, 1342226213		05h43m11.9s	-04d59m50s	D	x	

Source	Other Name	PACS OBSIDs	SPIRE OBSID	RA	Dec	Prog.	Jitter Corr.	SPIRE 1-D
HD 50138		1342206991, 1342206992		06h51m33.4s	-06d57m59s	D	x	
HD 97048		1342199412, 1342199413		11h08m03.3s	-77d39m18s	D	x	
HD 98922		1342210385		11h22m31.7s	-53d22m12s	D		
HH 100			1342252897	19h01m49.1s	-36d58m16.0s	C		
HH 46			1342245084	08h25m43.9s	-51d00m36.0s	C		x
HT Lup		1342213920		15h45m12.9s	-34d17m31s	D		
IRAM 04191+1522		1342216654, 1342216655		04h21m56.9s	+15d29m45.9s	D		
IRAS 03245+3002	L1455-IRS1	1342214677, 1342214676	1342249053	03h27m39.1s	+30d13m03.1s	D,C	x	x
IRAS 03301+3111	Perseus Bolo76	1342215668, 1342216181	1342249477	03h33m12.8s	+31d21m24.2s	D,C	x	x
IRAS 15398-3359	B228		1342250515	15h43m01.3s	-34d09m15.0s	C		x
IRS 46 / IRS44	Oph-IRS44/46	1342228474, 1342228475	1342251289	16h27m29.4s	-24d39m16.1s	D,C		
IRS 48	Oph-IRS48	1342227069, 1342227070		16h27m37.2s	-24d30m35s	D	x	
IRS 63	Oph-IRS63	1342228473, 1342228472		16h31m35.6s	-24d01m29.3s	D	x	
L1014		1342208911, 1342208912	1342245857	21h24m07.5s	+49d59m09.0s	D,C		x
L1157		1342208909, 1342208908	1342247625	20h39m06.3s	+68d02m16.0s	D,C	x	x
L1448-MM		1342213683, 1342214675		03h25m38.9s	+30d44m05.4s	D	x	x
L1455-IRS3	IRAS 03249+2957	1342204122, 1342204123	1342249474	03h28m00.4s	+30d08m01.3s	D,C		x

Source	Other Name	PACS OBSIDs	SPIRE OBSID	RA	Dec	Prog.	Jitter Corr.	SPIRE 1-D
L1489	IRAS 04016+2610	1342216216, 1342216215		04h04m42.9s	+26d18m56.3s	D	x	
L1527	IRAS 04368+2557	1342192981, 1342192982		04h39m53.9s	+26d03m09.8s	D	x	
L1551-IRS5		1342192805, 1342229711	1342249470	04h31m34.1s	+18d08m04.9s	D,C	x	x
L483	IRAS 18140-0440		1342253649	18h17m29.9s	-04d39m39.5s	C		x
L723-MM			1342245094	19h17m53.7s	+19d12m20.0s	C		x
RCrA-IRS5A		1342207806, 1342207805	1342253646	19h01m48.1s	-36d57m22.7s	D,C		x
RCrA-IRS7B		1342207807, 1342207808	1342242620	19h01m56.4s	-36d57m28.3s	D,C	x	x
RCrA-IRS7C		1342206990, 1342206989	1342242621	19h01m55.3s	-36d57m17.0s	D,C		x
RNO 90		1342228206		16h34m09.2s	-15d48m17s	D	x	
RNO 91			1342251285	16h34m29.3s	-15d47m01.4s	C		x
RU Lup		1342215682		15h56m42.3s	-37d49m16s	D	x	
RY Lup		1342216171		15h59m28.4s	-40d21m51s	D	x	
S Cra		1342207809, 1342207810		19h01m08.6s	-36d57m20s	D	x	
Serpens-SMM3		1342193216, 1342193214		18h29m59.3s	+01d14m01.7s	D	x	
Serpens-SMM4		1342193217, 1342193215		18h29m56.7s	+01d13m17.2s	D		
SR 21		1342227209, 1342227210		16h27m10.3s	-24d19m13s	D	x	
TMC 1A	IRAS 04362+2535	1342192987, 1342192988	1342250510	04h39m35.0s	+25d41m45.5s	D,C	x	x

Source	Other Name	PACS OBSIDs	SPIRE OBSID	RA	Dec	Prog.	Jitter Corr.	SPIRE 1-D
TMC 1	IRAS 04381+2540	1342225803, 1342225804	1342250512	04h41m12.7s	+25d46m35.9s	D,C	x	x
TMR 1	IRAS 04361+2547	1342192985, 1342192986	1342250509	04h39m13.9s	+25d53m20.6s	D,C	x	x
V1057 Cyg		1342235853, 1342235852	1342221695	20h58m53.7s	+44d15m29s	F	x	x
V1331 Cyg		1342233446, 1342233445	1342221694	21h01m09.2s	+50d21m45s	F	x	x
V1515 Cyg		1342235691, 1342235690	1342221685	20h23m48.0s	+42d12m26s	F	x	x
V1735 Cyg	Elias 1-12	1342235849, 1342235848	1342219560	21h47m20.7s	+47d32m04s	F	x	
VLA1623-243		1342213918, 1342213917	1342251287	16h26m26.4s	-24d24m30.0s	D,C	x	x
WL 12		1342228187, 1342228188	1342251290	16h26m44.2s	-24d34m48.4s	D,C	x	x

Table 1:: Contents of the archive organized by source. The ‘Prog.’ column refers to the first program in which the source was observed, where D = DIGIT, F = FOOSH, and C = COPS. The ‘Jitter Corr.’ column indicates the accessibility of the jitter corrected data. Sources with an ‘x’ in this column use the jitter-corrected products. The ‘SPIRE 1-D’ column indicates the accessibility of SPIRE extended calibrated 1-D spectra.

TABLE 2:: Line list for single Gaussian fitting: o-H₂O

Wavelength (μm)	Line name	Wavelength (μm)	Line name
55.13238	o-H ₂ O 8 ₂₇ – 7 ₁₆	55.84108	o-H ₂ O 10 ₂₉ – 10 ₁₁₀
56.81777	o-H ₂ O 9 ₀₉ – 8 ₁₈	57.39511	o-H ₂ O 7 ₅₂ – 8 ₂₇
58.70051	o-H ₂ O 4 ₃₂ – 3 ₂₁	61.31782	o-H ₂ O 5 ₄₁ – 6 ₁₆
62.92979	o-H ₂ O 9 ₁₈ – 9 ₀₉	63.32514	o-H ₂ O 8 ₁₈ – 7 ₀₇
63.91602	o-H ₂ O 6 ₆₁ – 6 ₅₂	63.95796	o-H ₂ O 7 ₆₁ – 7 ₅₂
65.16779	o-H ₂ O 6 ₂₅ – 5 ₁₄	66.09434	o-H ₂ O 7 ₁₆ – 6 ₂₅
66.43937	o-H ₂ O 3 ₃₀ – 2 ₂₁	67.27067	o-H ₂ O 3 ₃₀ – 3 ₀₃
70.70435	o-H ₂ O 8 ₂₇ – 8 ₁₈	71.94881	o-H ₂ O 7 ₀₇ – 6 ₁₆
74.94690	o-H ₂ O 7 ₂₅ – 6 ₃₄	75.38257	o-H ₂ O 3 ₂₁ – 2 ₁₂
75.49740	o-H ₂ O 8 ₅₄ – 8 ₄₅	75.83188	o-H ₂ O 6 ₅₂ – 6 ₄₃
75.91180	o-H ₂ O 5 ₅₀ – 5 ₄₁	77.76345	o-H ₂ O 7 ₅₂ – 7 ₄₃
78.74431	o-H ₂ O 4 ₂₃ – 3 ₁₂	81.40747	o-H ₂ O 9 ₂₇ – 9 ₁₈
82.03351	o-H ₂ O 6 ₁₆ – 5 ₀₅	82.97879	o-H ₂ O 8 ₃₆ – 8 ₂₇
84.76907	o-H ₂ O 7 ₁₆ – 7 ₀₇	85.77088	o-H ₂ O 8 ₄₅ – 8 ₃₆
92.81312	o-H ₂ O 6 ₄₃ – 6 ₃₄	94.64643	o-H ₂ O 6 ₂₅ – 6 ₁₆
94.70758	o-H ₂ O 4 ₄₁ – 4 ₃₂	104.09629	o-H ₂ O 6 ₃₄ – 6 ₂₅
108.07588	o-H ₂ O 2 ₂₁ – 1 ₁₀	112.51342	o-H ₂ O 7 ₄₃ – 7 ₃₄
112.80576	o-H ₂ O 4 ₄₁ – 5 ₁₄	113.54021	o-H ₂ O 4 ₁₄ – 3 ₀₃
114.45656	o-H ₂ O 9 ₂₇ – 10 ₁₁₀	116.35288	o-H ₂ O 8 ₃₆ – 9 ₀₉
116.78196	o-H ₂ O 7 ₃₄ – 6 ₄₃	121.72477	o-H ₂ O 4 ₃₂ – 4 ₂₃
123.46352	o-H ₂ O 9 ₃₆ – 9 ₂₇	127.88735	o-H ₂ O 7 ₂₅ – 7 ₁₆
129.34220	o-H ₂ O 9 ₄₅ – 9 ₃₆	132.41173	o-H ₂ O 4 ₂₃ – 4 ₁₄
133.55242	o-H ₂ O 8 ₃₆ – 7 ₄₃	134.93863	o-H ₂ O 5 ₁₄ – 5 ₀₅
136.49943	o-H ₂ O 3 ₃₀ – 3 ₂₁	156.26908	o-H ₂ O 5 ₂₃ – 4 ₃₂
159.05453	o-H ₂ O 8 ₄₅ – 7 ₅₂	159.40427	o-H ₂ O 6 ₃₄ – 7 ₀₇
160.51410	o-H ₂ O 5 ₃₂ – 5 ₂₃	166.81885	o-H ₂ O 7 ₃₄ – 7 ₂₅
174.63028	o-H ₂ O 3 ₀₃ – 2 ₁₂	174.92441	o-H ₂ O 4 ₃₂ – 5 ₀₅
179.53118	o-H ₂ O 2 ₁₂ – 1 ₀₁	180.49281	o-H ₂ O 2 ₂₁ – 2 ₁₂
187.81488	o-H ₂ O 8 ₅₄ – 9 ₂₇	212.53093	o-H ₂ O 5 ₂₃ – 5 ₁₄
226.76647	o-H ₂ O 6 ₂₅ – 5 ₃₂	229.21129	o-H ₂ O 8 ₄₅ – 9 ₁₈
231.25379	o-H ₂ O 8 ₂₇ – 7 ₃₄	234.53645	o-H ₂ O 7 ₄₃ – 6 ₅₂
256.59928	o-H ₂ O 8 ₅₄ – 7 ₆₁	257.80114	o-H ₂ O 3 ₂₁ – 3 ₁₂
258.82221	o-H ₂ O 6 ₃₄ – 5 ₄₁	259.98875	o-H ₂ O 3 ₁₂ – 2 ₂₁
261.46379	o-H ₂ O 7 ₂₅ – 8 ₁₈	273.19988	o-H ₂ O 3 ₁₂ – 3 ₀₃
483.00214	o-H ₂ O 5 ₃₂ – 4 ₄₁	538.30236	o-H ₂ O 1 ₁₀ – 1 ₀₁

TABLE 3:: Line list for single Gaussian fitting: p-H₂O

Wavelength (μm)	Line name	Wavelength (μm)	Line name
55.85970	p-H ₂ O 6 ₅₁ – 7 ₂₆	55.98480	p-H ₂ O 7 ₇₁ – 7 ₆₂
56.02824	p-H ₂ O 10 ₁₉ – 10 ₀₁₀	56.32640	p-H ₂ O 4 ₃₁ – 3 ₂₂
56.77240	p-H ₂ O 9 ₁₉ – 8 ₀₈	57.63798	p-H ₂ O 4 ₂₂ – 3 ₁₃
57.71080	p-H ₂ O 8 ₁₇ – 7 ₂₆	58.37824	p-H ₂ O 6 ₄₂ – 7 ₁₇
59.98863	p-H ₂ O 7 ₂₆ – 6 ₁₅	60.16365	p-H ₂ O 8 ₂₆ – 7 ₃₅
60.23082	p-H ₂ O 7 ₆₂ – 8 ₃₅	61.81016	p-H ₂ O 4 ₃₁ – 4 ₀₄
61.91772	p-H ₂ O 4 ₄₀ – 5 ₁₅	62.43311	p-H ₂ O 9 ₂₈ – 9 ₁₉
63.45961	p-H ₂ O 8 ₀₈ – 7 ₁₇	63.88177	p-H ₂ O 7 ₆₂ – 7 ₅₃
67.09082	p-H ₂ O 3 ₃₁ – 2 ₂₀	71.06907	p-H ₂ O 5 ₂₄ – 4 ₁₃
71.54146	p-H ₂ O 7 ₁₇ – 6 ₀₆	71.78955	p-H ₂ O 5 ₅₁ – 6 ₂₄
72.03407	p-H ₂ O 8 ₁₇ – 8 ₀₈	73.61471	p-H ₂ O 9 ₃₇ – 9 ₂₈
75.78324	p-H ₂ O 5 ₅₁ – 5 ₄₂	75.81532	p-H ₂ O 7 ₅₃ – 7 ₄₄
76.42386	p-H ₂ O 6 ₅₁ – 6 ₄₂	78.93042	p-H ₂ O 6 ₁₅ – 5 ₂₄
80.22431	p-H ₂ O 9 ₄₆ – 9 ₃₇	80.55884	p-H ₂ O 8 ₅₃ – 8 ₄₄
81.21765	p-H ₂ O 7 ₂₆ – 7 ₁₇	81.69220	p-H ₂ O 8 ₃₅ – 7 ₄₄
83.28606	p-H ₂ O 6 ₀₆ – 5 ₁₅	89.99061	p-H ₂ O 3 ₂₂ – 2 ₁₁
90.05205	p-H ₂ O 7 ₄₄ – 7 ₃₅	94.21193	p-H ₂ O 5 ₄₂ – 5 ₃₃
103.91892	p-H ₂ O 6 ₄₂ – 6 ₃₃	103.94278	p-H ₂ O 6 ₁₅ – 6 ₀₆
111.63078	p-H ₂ O 5 ₂₄ – 5 ₁₅	113.95081	p-H ₂ O 5 ₃₃ – 5 ₂₄
117.68692	p-H ₂ O 9 ₄₆ – 8 ₅₃	118.40826	p-H ₂ O 9 ₃₇ – 8 ₄₄
122.52519	p-H ₂ O 8 ₄₄ – 8 ₃₅	125.35683	p-H ₂ O 4 ₀₄ – 3 ₁₃
126.71711	p-H ₂ O 3 ₃₁ – 3 ₂₂	130.32199	p-H ₂ O 7 ₅₃ – 8 ₂₆
137.68652	p-H ₂ O 7 ₃₅ – 8 ₀₈	138.53127	p-H ₂ O 3 ₁₃ – 2 ₀₂
138.64412	p-H ₂ O 8 ₄₄ – 7 ₅₃	144.52144	p-H ₂ O 4 ₁₃ – 3 ₂₂
146.92643	p-H ₂ O 4 ₃₁ – 4 ₂₂	148.71156	p-H ₂ O 8 ₃₅ – 8 ₂₆
148.79410	p-H ₂ O 5 ₄₂ – 6 ₁₅	156.19792	p-H ₂ O 3 ₂₂ – 3 ₁₃
158.31551	p-H ₂ O 3 ₃₁ – 4 ₀₄	159.48926	p-H ₂ O 8 ₂₆ – 9 ₁₉
167.03912	p-H ₂ O 6 ₂₄ – 6 ₁₅	169.74305	p-H ₂ O 7 ₃₅ – 6 ₄₂
170.14342	p-H ₂ O 6 ₃₃ – 6 ₂₄	174.61126	p-H ₂ O 5 ₃₃ – 6 ₀₆
187.11543	p-H ₂ O 4 ₁₃ – 4 ₀₄	208.08146	p-H ₂ O 7 ₂₆ – 6 ₃₃
208.91861	p-H ₂ O 9 ₄₆ – 10 ₁₉	222.95328	p-H ₂ O 7 ₄₄ – 8 ₁₇
243.98004	p-H ₂ O 2 ₂₀ – 2 ₁₁	248.25302	p-H ₂ O 4 ₂₂ – 4 ₁₃
251.75737	p-H ₂ O 8 ₅₃ – 7 ₆₂	255.68729	p-H ₂ O 7 ₄₄ – 6 ₅₁
269.27908	p-H ₂ O 1 ₁₁ – 0 ₀₀	303.46381	p-H ₂ O 2 ₀₂ – 1 ₁₁
308.97175	p-H ₂ O 5 ₂₄ – 4 ₃₁	327.23126	p-H ₂ O 4 ₂₂ – 3 ₃₁
330.82984	p-H ₂ O 9 ₂₈ – 8 ₃₅	398.65260	p-H ₂ O 2 ₁₁ – 2 ₀₂
613.72660	p-H ₂ O 6 ₂₄ – 7 ₁₇	631.57098	p-H ₂ O 5 ₃₃ – 4 ₄₀
636.66801	p-H ₂ O 6 ₄₂ – 5 ₅₁		

TABLE 4:: Line list for single Gaussian fitting: CO and ^{13}CO

CO		^{13}CO	
Wavelength (μm)	Line name	Wavelength (μm)	Line name
54.98622	CO $J = 48 \rightarrow 47$	209.48144	$^{13}\text{CO } J = 13 \rightarrow 12$
56.12190	CO $J = 47 \rightarrow 46$	226.90368	$^{13}\text{CO } J = 12 \rightarrow 11$
57.30773	CO $J = 46 \rightarrow 45$	247.49662	$^{13}\text{CO } J = 11 \rightarrow 10$
58.54705	CO $J = 45 \rightarrow 44$	272.21148	$^{13}\text{CO } J = 10 \rightarrow 9$
59.84349	CO $J = 44 \rightarrow 43$	302.42221	$^{13}\text{CO } J = 9 \rightarrow 8$
61.20106	CO $J = 43 \rightarrow 42$	340.18978	$^{13}\text{CO } J = 8 \rightarrow 7$
62.62410	CO $J = 42 \rightarrow 41$	388.75282	$^{13}\text{CO } J = 7 \rightarrow 6$
64.11741	CO $J = 41 \rightarrow 40$	453.50906	$^{13}\text{CO } J = 6 \rightarrow 5$
65.68791	CO $J = 40 \rightarrow 39$	544.17444	$^{13}\text{CO } J = 5 \rightarrow 4$
67.33814	CO $J = 39 \rightarrow 38$		
69.07614	CO $J = 38 \rightarrow 37$		
70.90902	CO $J = 37 \rightarrow 36$		
72.84469	CO $J = 36 \rightarrow 35$		
74.89194	CO $J = 35 \rightarrow 34$		
77.06064	CO $J = 34 \rightarrow 33$		
79.36181	CO $J = 33 \rightarrow 32$		
81.80787	CO $J = 32 \rightarrow 31$		
84.41284	CO $J = 31 \rightarrow 30$		
87.19261	CO $J = 30 \rightarrow 29$		
90.16527	CO $J = 29 \rightarrow 28$	173.63580	CO $J = 15 \rightarrow 14$
93.35147	CO $J = 28 \rightarrow 27$	186.00397	CO $J = 14 \rightarrow 13$
104.44758	CO $J = 25 \rightarrow 24$	200.27751	CO $J = 13 \rightarrow 12$
108.76555	CO $J = 24 \rightarrow 23$	216.93275	CO $J = 12 \rightarrow 11$
113.46045	CO $J = 23 \rightarrow 22$	236.61924	CO $J = 11 \rightarrow 10$
118.58370	CO $J = 22 \rightarrow 21$	260.24634	CO $J = 10 \rightarrow 9$
124.19648	CO $J = 21 \rightarrow 20$	289.12761	CO $J = 9 \rightarrow 8$
130.37221	CO $J = 20 \rightarrow 19$	325.23335	CO $J = 8 \rightarrow 7$
137.19978	CO $J = 19 \rightarrow 18$	371.65974	CO $J = 7 \rightarrow 6$
144.78783	CO $J = 18 \rightarrow 17$	433.56713	CO $J = 6 \rightarrow 5$
153.27056	CO $J = 17 \rightarrow 16$	520.24412	CO $J = 5 \rightarrow 4$
162.81572	CO $J = 16 \rightarrow 15$	650.26787	CO $J = 4 \rightarrow 3$

TABLE 5:: Line list for single Gaussian fitting: OH, HCO⁺, and CH⁺

OH		HCO ⁺ & CH ⁺	
Wavelength (μm)	Line name	Wavelength (μm)	Line name
55.89231	OH ${}^2\Pi_{1/2, 9/2}^+ - {}^2\Pi_{1/2, 7/2}^-$	210.28817	HCO ⁺ $J = 16 \rightarrow 15$
55.95141	OH ${}^2\Pi_{1/2, 9/2}^- - {}^2\Pi_{1/2, 7/2}^+$	224.28136	HCO ⁺ $J = 15 \rightarrow 14$
65.13337	OH ${}^2\Pi_{3/2, 9/2}^- - {}^2\Pi_{3/2, 7/2}^+$	240.27541	HCO ⁺ $J = 14 \rightarrow 13$
65.28048	OH ${}^2\Pi_{3/2, 9/2}^+ - {}^2\Pi_{3/2, 7/2}^-$	258.73207	HCO ⁺ $J = 13 \rightarrow 12$
71.17262	OH ${}^2\Pi_{1/2, 7/2}^- - {}^2\Pi_{1/2, 5/2}^+$	280.26712	HCO ⁺ $J = 12 \rightarrow 11$
71.21723	OH ${}^2\Pi_{1/2, 7/2}^+ - {}^2\Pi_{1/2, 5/2}^-$	305.71952	HCO ⁺ $J = 11 \rightarrow 10$
79.11754	OH ${}^2\Pi_{1/2, 1/2}^- - {}^2\Pi_{3/2, 3/2}^+$	336.26531	HCO ⁺ $J = 10 \rightarrow 9$
79.18106	OH ${}^2\Pi_{1/2, 1/2}^+ - {}^2\Pi_{3/2, 3/2}^-$	373.60195	HCO ⁺ $J = 9 \rightarrow 8$
84.42237	OH ${}^2\Pi_{3/2, 7/2}^+ - {}^2\Pi_{3/2, 5/2}^-$	420.27521	HCO ⁺ $J = 8 \rightarrow 7$
84.59877	OH ${}^2\Pi_{3/2, 7/2}^- - {}^2\Pi_{3/2, 5/2}^+$	480.28810	HCO ⁺ $J = 7 \rightarrow 6$
115.15057	OH ${}^2\Pi_{1/2, 5/2}^+ - {}^2\Pi_{3/2, 7/2}^-$	560.30913	HCO ⁺ $J = 6 \rightarrow 5$
115.38441	OH ${}^2\Pi_{1/2, 5/2}^- - {}^2\Pi_{3/2, 7/2}^+$	60.24659	CH ⁺ $J = 6 \rightarrow 5$
119.23740	OH ${}^2\Pi_{3/2, 5/2}^- - {}^2\Pi_{3/2, 3/2}^+$	72.13950	CH ⁺ $J = 5 \rightarrow 4$
119.44450	OH ${}^2\Pi_{3/2, 5/2}^+ - {}^2\Pi_{3/2, 3/2}^-$	119.85466	CH ⁺ $J = 3 \rightarrow 2$
134.84152	OH ${}^2\Pi_{1/2, 7/2}^- - {}^2\Pi_{3/2, 9/2}^+$	358.99894	CH ⁺ $J = 1 \rightarrow 0$
135.95981	OH ${}^2\Pi_{1/2, 7/2}^+ - {}^2\Pi_{3/2, 9/2}^-$		
154.78349	OH ${}^2\Pi_{1/2, 9/2}^+ - {}^2\Pi_{3/2, 11/2}^-$		
157.80984	OH ${}^2\Pi_{1/2, 9/2}^- - {}^2\Pi_{3/2, 11/2}^+$		
163.12467	OH ${}^2\Pi_{1/2, 3/2}^+ - {}^2\Pi_{1/2, 1/2}^-$		
163.40013	OH ${}^2\Pi_{1/2, 3/2}^- - {}^2\Pi_{1/2, 1/2}^+$		

Note—The notation of OH transition follows the form of ${}^2\Pi_{J_e, J_{\text{total}}}^{\text{parity}}$. J_e is the electron angular momentum quantum number, while J_{total} is the total angular momentum quantum number including electron and nuclear rotation. Please see more detail of the 163.12467 μm OH line in §4.1.

TABLE 6:: Line list for single Gaussian fitting: atomic fine-structure lines

Wavelength (μm)	Line name	Wavelength (μm)	Line name
63.18367	[O I] $^3\text{P}_1 - ^3\text{P}_2$	121.911 \pm 0.006 ^a	[N II] $^3\text{P}_2 - ^3\text{P}_1$
145.48056	[O I] $^3\text{P}_0 - ^3\text{P}_1$	157.69228	[C II] $^2\text{P}_{3/2} - ^2\text{P}_{1/2}$
205.170 \pm 0.004 ^a	[N II] $^3\text{P}_1 - ^3\text{P}_0$	230.34913	[C I] $^3\text{P}_2 - ^3\text{P}_0$
370.42438	[C I] $^3\text{P}_2 - ^3\text{P}_1$	609.15069	[C I] $^3\text{P}_1 - ^3\text{P}_0$

^a The mean values and the standard deviation of the mean of line centroids are measured from the corresponding fitted lines with SNR > 10. The initial guesses were 121.9 μm , and 205.178 μm .

TABLE 7:: Blended lines fit with double Gaussian profile

Wavelength (μm)	Line names
55.85970 55.89231	p-H ₂ O 6 ₅₁ - 7 ₂₆ OH $^2\Pi_{1/2, 9/2}^+ - ^2\Pi_{1/2, 7/2}^-$
55.95141 55.98480	OH $^2\Pi_{1/2, 9/2}^- - ^2\Pi_{1/2, 7/2}^+$ p-H ₂ O 7 ₇₁ - 7 ₆₂
56.77240 56.81777	p-H ₂ O 9 ₁₉ - 8 ₀₈ o-H ₂ O 9 ₀₉ - 8 ₁₈
65.13337 65.16779	OH $^2\Pi_{3/2, 9/2}^- - ^2\Pi_{3/2, 7/2}^+$ o-H ₂ O 6 ₂₅ - 5 ₁₄
71.17262 71.21723	OH $^2\Pi_{1/2, 7/2}^- - ^2\Pi_{1/2, 5/2}^+$ OH $^2\Pi_{1/2, 7/2}^+ - ^2\Pi_{1/2, 5/2}^-$
75.81532 75.83188	p-H ₂ O 7 ₅₃ - 7 ₄₄ o-H ₂ O 6 ₅₂ - 6 ₄₃
79.11754 79.18106	OH $^2\Pi_{1/2, 1/2}^- - ^2\Pi_{3/2, 3/2}^+$ OH $^2\Pi_{1/2, 1/2}^+ - ^2\Pi_{3/2, 3/2}^-$
84.41284 84.42237	CO $J = 31 \rightarrow 30$ OH $^2\Pi_{3/2, 7/2}^+ - ^2\Pi_{3/2, 5/2}^-$
113.46045 113.54021	CO $J = 23 \rightarrow 22$ o-H ₂ O 4 ₁₄ - 3 ₀₃
118.40826 118.58370	p-H ₂ O 9 ₃₇ - 8 ₄₄ CO $J = 22 \rightarrow 21$
130.32199 130.37221	CO $J = 20 \rightarrow 19$ p-H ₂ O 7 ₅₃ - 8 ₂₆
134.84152 134.93863	OH $^2\Pi_{1/2, 7/2}^- - ^2\Pi_{3/2, 9/2}^+$ o-H ₂ O 5 ₁₄ - 5 ₀₅
156.19792 156.26908	p-H ₂ O 3 ₂₂ - 3 ₁₃ o-H ₂ O 5 ₂₃ - 4 ₃₂
144.52144 144.78783	p-H ₂ O 4 ₁₃ - 3 ₂₂ CO $J = 18 \rightarrow 17$
166.81885 167.03912	o-H ₂ O 7 ₃₄ - 7 ₂₅ p-H ₂ O 6 ₂₄ - 6 ₁₅
174.61126 174.63028	p-H ₂ O 5 ₃₃ - 6 ₀₆ o-H ₂ O 3 ₀₃ - 2 ₁₂
259.98875 260.24634	o-H ₂ O 3 ₁₂ - 2 ₂₁ CO $J = 10 \rightarrow 9$
272.21148 273.19988	¹³ CO $J = 10 \rightarrow 9$ o-H ₂ O 3 ₁₂ - 3 ₀₃
302.42221 303.46381	¹³ CO $J = 9 \rightarrow 8$ p-H ₂ O 2 ₀₂ - 1 ₁₁
370.42438 371.65974	[C I] $^3\text{P}_2 - ^3\text{P}_1$ CO $J = 7 \rightarrow 6$
609.15069 613.72660	[C I] $^3\text{P}_1 - ^3\text{P}_0$ p-H ₂ O 6 ₂₄ - 7 ₁₇

TABLE 8.: A portion of the 1-D spectrum fitting results for BHR71. The tables in the ASCII files have the same columns and style except that the rows are chopped into three parts here for better display. Also this table has selected lines from different parts of the original results to demonstrate different flags, etc. As mentioned in §4.6, any column with -999 indicates a fitting result that is not well-constrained. Therefore, the Validity flag is set to be 0. The Pixel_No. column lists “c” for the 1-D spectrum measurements, and the specific pixel number/name for cube measurements. This table (all line measurements for all sources) is published in its entirety in the electronic edition.

Line	LabWL (um)	ObsWL (um)	Sig_Cen (um)	Str (W/cm2)	Sig_str (W/cm2)	
CO48-47	54.98621750	54.98154779	0.03082777749	-2.277802385e-21	2.967605715e-21	
p-H2O4.31-3.22	56.32640076	56.30309023	0.007689705798	8.970946845e-21	2.958435088e-21	
CO46-45	57.30772781	57.30463621	0.2850716473	-2.699435981e-22	3.260885618e-21	
o-H2O6.61-6.52	63.91602325	63.93649292	-999.0000000	2.197260987e-21	2.763702731e-21	
o-H2O7.61-7.52	63.95696259	63.93729134	0.02943608129	2.198141514e-21	2.764042837e-21	
p-H2O9.37-8.44	118.4082565	118.4959793	-999.0000000	3.497948853e-20	1.314679686e-20	
CO22-21	118.5837021	118.5876394	0.003691032704	7.394416427e-20	3.865617628e-21	
p-H2O8.35-8.26	148.7115631	148.7528381	-999.0000000	-3.672127599e-21	1.629373707e-21	
CO4-3	650.2678833	650.2828864	0.01499258376	4.128831785e-20	6.530348726e-22	
CI3P2-3P1	370.4243774	370.4243774	-998.0000000	0.000000000	-998.0000000	
FWHM (um)	Sig_FWHM (um)	Base (W/cm2/um)	Noise (W/cm2/um)	SNR	E_u (K)	
0.03897858372	-998.0000000	5.860891006e-18	8.720767999e-20	0.6297869004	6457.230000	
0.03906316840	-998.0000000	6.295500447e-18	8.226700068e-20	2.623635637	552.3000000	
0.03912018226	-998.0000000	6.354233016e-18	1.049475567e-19	0.06179569179	5939.210000	
0.03936703190	-998.0000000	7.381455348e-18	6.509757235e-20	0.8058283595	1503.600000	
0.03936783131	-998.0000000	7.381706869e-18	7.165146509e-20	0.7323985066	1749.900000	
0.1169993003	-998.0000000	6.777696602e-18	9.334557437e-20	3.010196356	1749.900000	
0.1170676737	-998.0000000	6.772795551e-18	3.430364591e-20	17.305533393	1397.380000	
0.1251977122	-998.0000000	4.240183287e-18	1.615138300e-20	1.706750436	1511.000000	
2.951818452	0.03529221031	1.568093311e-20	3.629903522e-22	36.21602920	55.32000000	
0.9943682530	-998.0000000	2.116988821e-19	1.348351580e-21	0.000000000	62.46200000	
A (s-1)	g	RA (deg)	Dec (deg)	Pixel_No.	Blend	Validity
0.006556000000	97	180.3982553	-65.14761521	c	x	1
1.452000000	9	180.3982553	-65.14761521	c	x	1
0.006091000000	93	180.3982553	-65.14761521	c	x	1
0.3533000000	39	180.3982553	-65.14761521	c	Red	0
0.5828000000	45	180.3982553	-65.14761521	c	Red/Blue	0
0.017240000000	19	180.3982553	-65.14761521	c	Red	0
0.001006000000	45	180.3982553	-65.14761521	c	Red/Blue	1
0.1235000000	17	180.3982553	-65.14761521	c	Red	0
6.126000000e-06	9	180.4010925	-65.14799500	c	x	1
2.650000000e-07	5	180.4010925	-65.14799500	c	DoubleGaussian	1